

Defect Tolerance of Lead-Halide Perovskite (100) Surface Relative to Bulk: Band Bending, Surface States, and Characteristics of Vacancies

Published as part of *The Journal of Physical Chemistry C virtual special issue "The Physical Chemistry of Perovskites."*

Oleg Rubel* and Xavier Rocquefelte



Cite This: *J. Phys. Chem. C* 2024, 128, 5667–5679



Read Online

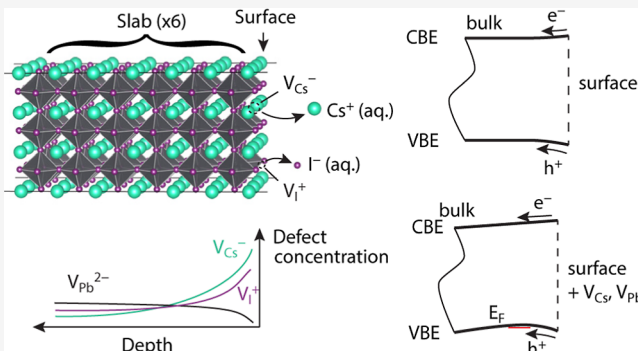
ACCESS |

Metrics & More

Article Recommendations

Supporting Information

ABSTRACT: We characterized the formation of vacancies at a surface slab model and contrasted the results with the bulk of lead-halide perovskites by using cubic and tetragonal CsPbI_3 as representative structures. The defect-free CsI-terminated (100) surface does not trap charge carriers. In the presence of defects (vacancies), the surface is expected to exhibit a *p*-type behavior. The formation energy of cesium vacancies V_{Cs}^- is lower at the surface than in the bulk, while iodine vacancies V_{I}^+ have a similar energy (around 0.25–0.4 eV) within the range of chemical potentials compatible with solution processing synthesis conditions. Lead–iodine divacancies (V_{PbI}^-) are expected to dominate lead-only vacancies at the surfaces. Major surface vacancies create shallow host-like energy states with a small Franck–Condon shift, making them electronically harmless (same as in bulk). The spin–orbit coupling contributes to the defect tolerance of lead-halide perovskite surfaces by causing delocalization of electronic states associated with *n*-type defects and retraction of the lowest unoccupied states from the surface due to a mixing of $\text{Pb}_{x,y,z}$ orbitals. These results explain a high optoelectronic performance of two-dimensional structures, nanoparticles, and polycrystalline thin films of lead-halide perovskites despite the abundance of interfaces in these materials.



Downloaded via MCMMASTER UNIV on September 17, 2025 at 20:21:19 (UTC).
See https://pubs.acs.org/sharingguidelines for options on how to legitimately share published articles.

INTRODUCTION

Electronic-structure approaches to modeling defects in solids allow us to predict formation energies of defects, defect concentrations at finite temperatures, and charge-state transition levels taking into account growth conditions and position of the Fermi energy in semiconductors.^{1,2} Most of the time, such calculations aim to characterize defects in the bulk of a material, which is modeled with periodic boundary conditions in all directions. Far fewer studies address the calculation of defects at interfaces, for example, heterointerfaces^{3,4} and surfaces.^{5,6} The presence of an interface alters characteristics of defects compared to the bulk by either changing the formation energy of defects (e.g., O^{2-} vacancy on the $\text{MgO}(110)$ surface is 0.2 eV more stable⁶), or by introducing new localized states (an N vacancy introduced interface states⁴), or by changing the defect concentration (segregation of oxygen vacancies³).

Single-crystal lead-halide perovskites (organic and inorganic) have a very low concentration of deep electronic traps,⁷ which is attributed to the “defect tolerance” of perovskite materials supported by numerous models.^{8–16} The “defect tolerance” is associated with shallow transition energy levels of

major native point defects in bulk. Interestingly, layered perovskites,¹⁷ nanoparticles,^{18,19} and polycrystalline thin films^{20,21} demonstrate good optoelectronic activity. This suggests that surfaces and grain boundaries are also not significant sources of deep electronic traps. Additional efforts are directed toward surface passivation to obtain photovoltaic devices with record-high efficiencies.^{22,23} Strategies for surface passivation include a reactive postgrowth treatment of the surface with larger organic cations to favor *n*-type doping versus typical *p*-type conductivity or intrinsic nature²⁴ resulting in a twofold extended lifetime of charge carriers.²⁵

Prior theoretical models^{26–28} of a methylammonium (MA) lead iodide (MAPbI_3) surface arrived at a general conclusion about the absence of deep level surface states within the band gap. However, the literature remains controversial with regard

Received: September 8, 2023

Revised: February 19, 2024

Accepted: March 7, 2024

Published: March 20, 2024



to the localization or delocalization of electronic states at the band edges in slab models. For instance, Buin et al.²⁶ reported the delocalization of electronic states at both band edges of a MAPbI₃ slab model simulated with the density functional theory (DFT). Haruyama et al.²⁷ modeled the band edges of a MAPbI₃(100) slab with various terminations and concluded that the valence band edge (VBE) states are localized at the surface, while the conduction band edge (CBE) states are delocalized under PbI termination conditions. Meggiolaro et al.²⁸ showed the attraction of CBE states to the (100) surface of MAI-terminated MAPbI₃ and the repulsion of VBE states. Stoumpos et al.²⁹ found that both VBE and CBE states of a Ruddlesden–Popper bulk phase [CH₃(CH₂)₃NH₃]₂(CH₃NH₃)₄Pb₅I₁₆ ($n = 5$) were strongly localized within one atomic layer near the surface (VBE and CBE states did not overlap in real space), while states at the band edges were absent within the slab.

The literature on the theoretical characterization of defects at the surface of perovskites is rather scarce and patchy. Mosconi et al.³⁰ alluded to a higher concentration of defect complexes (I_i⁻/V_i⁺ Frenkel pairs) at the surface of MAPbI₃ due to a lower formation energy of such defects at MAI-vacant or PbI-terminated surfaces but not at the regular MAI-terminated surface; the analysis is limited to charge-neutral configurations. Perez et al.³¹ recently concluded that 2D Ruddlesden–Popper perovskites (single-layer butylammonium lead iodide) generally retain their defect tolerance with a limited perturbation of the electronic structure (shallow states for iodine vacancy). This conclusion was derived from an analysis of changes in the density of states of structures with iodine, butylammonium, and PbI₂ vacancies, as well as iodine interstitials. Only the latter leads to deep localized states within the band gap.³¹ To ensure the robustness of their conclusions with respect to thermal fluctuations of ionic positions, the authors of ref 31 performed a molecular dynamics simulation of structures with defects up to 2 ps and sampled the electronic structure at several intermediate snapshots. ten Brinck et al.³² studied the neutral defect complexes in CsPbI₃ nanocrystals (nonperiodic models) without spin–orbit coupling (SOC) and obtained rather large formation energies (3–8 eV) of vacancies without much difference between bulk and the surface location. Most defect complexes that show a negative (or low positive) formation energy also form localized states in the gap,³² which could be attributed to peculiarities of charge balancing in a defect-free nanoparticle being intrinsically not insulating.

Song et al.³³ reported the most comprehensive comparison of defects' characteristics in slab versus bulk, and their approach appears closest to our work. The authors of ref 33 studied 12 native point defects in Ruddlesden–Popper butylammonium, MA lead iodide ($n = 1, 2, 3$, organic cations were modeled as Cs) at the DFT level without SOC. Shallow transition energy levels in 2D perovskites appeared deeper in the gap compared to the same levels in the bulk structure, and extended even deeper into the gap as defects approached the surface in 2D structures. Vacancies were the dominant defects with the lowest formation energy in both the bulk and in the 2D structure ($n = 3$). Counterintuitively, formation energies of neutral vacancies (V_{Cs} , V_{Pb} , and V_{I}) were 0.2–0.7 eV lower in bulk than at the surface of the Ruddlesden–Popper 2D layer ($n = 3$), which do not support the idea of defects segregating at the surface. It is worth noting that formation energies of the low-energy defects were always negative (regardless of the Fermi energy position or the selection of chemical potentials)

for all investigated structures,³³ which suggests spontaneous formation of defects in large quantities during synthesis.

Here, we perform a study of the most basic intrinsic surface defects (native vacancies) in cubic and tetragonal CsPbI₃ that serve as a computationally more efficient proxy for the structure of hybrid lead-halide perovskites under ambient conditions. We expect that these simple structures share essential properties of defects with more complex hybrid lead-halide perovskites, despite the cubic phase of CsPbI₃ being unstable at room temperature.³⁴ We calculate the formation energy at various charge states and transition energy levels of these defects by contrasting results for the surface versus the bulk. Since our slab models are equivalent to the 2D Ruddlesden–Popper structure with the number of layers $n = 5$ and 6 (tetragonal and cubic, respectively), we anticipate the results to also be transferable to layered perovskites. There are several features that differentiate our work from the prior art. (i) Our choice of chemical potentials of atomic species is tailored to the activity of aqueous ions, in order to best represent solution-processing growth conditions. (ii) We provide quantitative characteristics of the localization of defects' electronic states. (iii) We also elucidate the effect of SOC on the formation energy of defects and the location of transition energy levels. We identified defect characteristics and types for which SOC can (and cannot) be neglected. (iv) When studying the transition energy levels, we differentiate between thermodynamic energy levels and electronic transition levels by imposing limits on the structural relaxation (the Franck–Condon principle^{35,36}).

METHODS

Electronic structure calculations were performed using DFT^{37,38} at the Perdew, Burke, and Ernzerhof (PBE)³⁹ level of theory implemented in Vienna ab initio simulation package (VASP)^{40–42} (version 6.4.2). The DFT + D3 method with Becke–Johnson damping^{43,44} was used to capture long-range van der Waals interactions. Projector augmented wave pseudopotentials⁴⁵ with 9, 14, and 7 valence electrons were employed for Cs, Pb, and I, respectively. The plane wave cutoff energy was set at the upper limit specified by the pseudopotentials (238 eV). This choice of the cutoff energy gives defect formation energies converged to a precision of 0.1 eV, which was verified using a higher cutoff energy (297 eV) for neutral vacancies in bulk without SOC.

The Brillouin zone was sampled using a Γ -centered grid of k points⁴⁶ with a mesh density of $2 \times 2 \times 2$ for the bulk supercells of the size $4 \times 4 \times 4$ and $3\sqrt{2} \times 3\sqrt{2} \times 4$, the density of $2 \times 2 \times 1$ for the slab supercells of the size $3 \times 3 \times 6$ and $2\sqrt{2} \times 2\sqrt{2} \times 5$, the density of $3 \times 3 \times 1$ and $8 \times 8 \times 1$ for the slab supercells of the size $2 \times 2 \times 3$ and $1 \times 1 \times 6$, respectively. The k mesh was selected having the zone folding in mind, specifically, the $R(1/2, 1/2, 1/2)$ point with CBE and VBE of the primitive cubic Brillouin zone is folded into Γ in supercells with even multiplicity and into $M(1/2, 1/2, 0)$ in the slab model with odd multiplicity in the lateral directions. Γ and M points are included in our sampling. We tested the convergence of the total energy, defect formation energies, and transition energy levels with respect to the k mesh density and concluded that the Γ -only calculations (often practiced in the literature for large sizes of supercells) lead to inaccurate results. We also tested accuracy of the total energy computed with a tetrahedron integration method versus a Gaussian smearing of

0.01 eV (employed in this work) and found differences immaterial for defect characteristics.

The only dynamically stable structure of CsPbI_3 is the orthorhombic (δ) non-perovskite $Pnma$ phase.⁴⁷ However, its electronic structure is very distinct from tetragonal or cubic perovskite structures.^{48,49} For this reason, we selected cubic and tetragonal structures of CsPbI_3 , as computationally more efficient representatives of hybrid lead-halide perovskites, such as $(\text{CH}_3\text{NH}_3)\text{PbI}_3$, that has a tetragonal phase very close to cubic at room temperature.^{50–52} The initial structure of cubic CsPbI_3 ($Pm\bar{3}m$, no. 221, $a = 6.414 \text{ \AA}$) was obtained from the Materials Project⁵³ (ID 1069538). The calculated stress for the structure did not exceed 1 kbar; thus, the structure did not require an additional relaxation of the lattice parameters. The initial tetragonal structure of CsPbI_3 ($I4/mcm$, no. 140, $a = 8.749 \text{ \AA}$ and $c = 12.748 \text{ \AA}$) was constructed based on the tetragonal phase of $(\text{CH}_3\text{NH}_3)\text{PbI}_3$ ⁵⁰ and subsequently relaxed. The stress was also less than 1 kbar in the defect-free supercell and in the slab (in lateral directions), which allows us to fix the lattice and relax only atomic positions (when perturbed by a defect or surface reconstruction) to a desired force threshold. The energy and force convergence thresholds were set at 10^{-7} eV and $10^{-2} \text{ eV \AA}^{-1}$, respectively. A relatively tight force threshold was essential for convergence of the total energies (and defect formation energies eventually), given the large number of atoms in the supercells.

Calculations were performed with and without SOC. When SOC was included, the calculation was initialized in a zero spin configuration. A spin-unpolarized calculation mode was selected in the absence of SOC. Relaxation of atomic positions was done without SOC, and the relaxed structures were used in the calculations with SOC without additional force optimization to save computational time. The latter simplification leads to a maximum force still below $0.02\text{--}0.05 \text{ eV \AA}^{-1}$ after adding SOC. Heyd–Scuseria–Ernzerhof 2006 (HSE06)^{54,55} exchange–correlation (XC) functional in combination with SOC was used for benchmarking purposes on a small slab model to ensure the validity of conclusions drawn from PBE calculations that suffer from a large band gap error.

Thermodynamic properties of defects were analyzed using the PyDEF 2 code^{56,57} with minor modifications (see the fork at GitHub⁵⁸) that enable processing of VASP OUTCAR files when SOC is included and compatibility with VASP version 6. The formation energy of a defect D in a charge state q includes the following terms^{2,59,60}

$$E_d(D^q, \Delta E_F) = E_{\text{tot}}(D^q) - E_{\text{tot}}(\text{host}) \pm \sum_{\alpha} \mu(\alpha) + q[E_{\text{VBE}}(\text{host}) + \Delta E_F] + E_{\text{corr}} \quad (1)$$

where E_{tot} is the DFT total energy, μ is the chemical potential of each atomic species α added to (negative sign) or subtracted from (positive sign) the host cell, $E_{\text{VBE}}(\text{host})$ is the VBE eigenvalue of the host cell, ΔE_F defines the position of the Fermi energy relative to $E_{\text{VBE}}(\text{host})$, and E_{corr} is a correction term applied to $E_{\text{tot}}(D^q)$. We included the following corrections: (i) a filling of dispersive states in a finite-size supercell⁶⁰ (the Moss–Burstein effect), (ii) a potential alignment between the neutral host and the charged cell.⁶¹ We found that the inclusion of Makov and Payne⁶² monopole correction for charged bulk cells (VASP tag LMONO = T) computed with the dielectric permittivity of 6.3⁶³ (VASP tag

EPSILON = 6.3) has a minor effect on the total energy of $\pm 1e$ charged bulk structures (0.1 eV or less in the bulk model) but results in overcorrection of transition levels for shallow, dispersed host-like defect states, and it was eventually abandoned (see also the discussion in ref 60).

An electrostatic correction for charged defects in a slab is extensively discussed in the literature.^{5,64–67} The correction aims to compensate for a difference in the electrostatic potential energy U of an isolated charged defect in a slab relative to the electrostatic potential energy of the same defect in a periodic slab model⁶⁸

$$\delta U(q) = U_{\text{iso}}(q) - U_{\text{per}}(q) \quad (2)$$

(The potential alignment term is already included in the E_{corr} term in eq 1.) The electrostatic energy resulting from the additional charge q in the periodic model can be expressed as⁶⁸

$$U_{\text{per}} = \frac{1}{2} \int_{\text{cell}} \delta\phi(\mathbf{r}) \delta\rho(\mathbf{r}) \, d\mathbf{r} \quad (3)$$

where $\delta\rho(\mathbf{r})$ is the excess charge density and $\delta\phi(\mathbf{r})$ is the electrostatic potential due to the excess charge compatible with periodic boundary conditions and the dielectric function profile imposed by the slab model (see Figure S8 in the Supporting Information section). It is expected that the excess charge density distribution fulfills the following equation: $\int_{\text{cell}} \delta\rho(\mathbf{r}) \, d\mathbf{r} = q$. The periodic electrostatic energy for charged slab models U_{per} was calculated using the sxdefectalign2d package.^{65,69} In our case, the defect states are extended host-like states, and the charge q is delocalized in the lateral plane. Since the electrostatic energy of a charge q is inversely proportional to its spatial extent β for either two- or three-dimensional distribution,^{5,70} it is proposed to set $U_{\text{iso}} = 0$ in the limit of $\beta_{\parallel} \rightarrow \infty$, consistent with states delocalized in the lateral plane of the slab. This limit was also verified using sxdefectalign2d by increasing the lateral broadening to $\beta_{\parallel} = 200$ bohr and observing $\lim_{\beta_{\parallel} \rightarrow \infty} U_{\text{iso}} = 0$. For large slab models and the charge state of $q = \pm 1$, relevant for most defects studied here, the correction δU amounts to $-0.06\text{--}-0.11 \text{ eV}$. Since δU is a part of the correction term E_{corr} in eq 1, the effect of this correction on the formation energy of charged defects is rather minor (reduction by $-0.06\text{--}-0.11 \text{ eV}$).

An energy level corresponding to a transition between charge states q_1 and q_2 in the structure with a defect D is expressed as⁶¹

$$e(D^{q_1/q_2}) = \frac{E_d(D^{q_1}, 0) - E_d(D^{q_2}, 0)}{q_2 - q_1} \quad (4)$$

Calculations of the formation energy of ionized defects can be done either adiabatically (i.e., with structural relaxation) or following the Franck–Condon principle for electronic transitions (i.e., without structural relaxation). Here we present and discuss results obtained with both approaches. The VASP output and structure files used in defect calculations are available from the Zenodo repository⁷¹ along with PyDEF 2 output files.

VASP-generated PROCAR files were used to analyze the localization of the electronic states. The PROCAR output format was modified from the original VASP source code to ensure that the output of k -, band-, and atom-resolved probability densities had at least three significant digits. The prPROCAR.m Octave script from VASPTools (available on

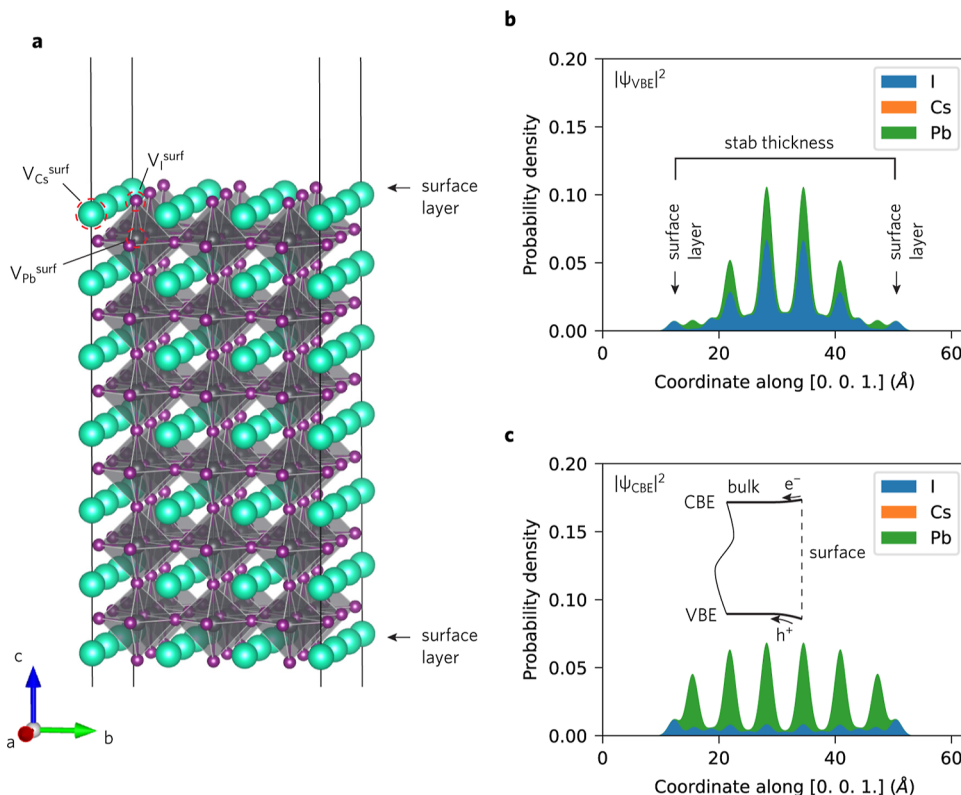


Figure 1. (a) Geometry of a $3 \times 3 \times 6$ cubic CsPbI_3 slab for modeling of (100) surface states. The model is periodic along a and b lattice vectors. Location of defects (vacancies) at the surfaces is indicated. (b,c) Spatial distribution of the atom-resolved (α) wave function probability density $|\psi_{n,k,\alpha}|^2$ for the band index n and the wave vector k that correspond to the band edges VBE and CBE of the slab model. Contributions of individual atoms in a plane with a coordinate z are stacked on top of each other. SOC is included. A Gaussian smearing of $\sigma = 1 \text{ \AA}$ is applied to all atoms.

GitHub⁷²) was employed to extract the k - and band-resolved participation ratio (PR) data.

RESULTS AND DISCUSSION

Structural Model and Surface States. An atomistic model of the (100) surface (also employed later for studying defects) is shown in Figure 1a. The model features a slab with a thickness equivalent to six $[\text{PbI}_6]$ octahedra, CsI surface termination, and periodic boundary conditions in two lateral directions. The structure is equivalent to a two-dimensional version of a Ruddlesden–Popper phase⁷³ with the composition $9\text{Cs}_7\text{Pb}_6\text{I}_{19}$ that falls into a general formula $A_{n+1}B_nX_{3n+1}$ with $n = 6$. The factor of 9 reflects 3×3 supercell multipliers in the lateral plane. The vacuum region of ca. 25 Å prevents any spurious interaction between periodic images in the direction z perpendicular to the surface. We deliberately selected a structure with the inorganic cation (Cs^+) instead of its organic counterparts (e.g., CH_3NH_3^+). Organic molecules introduce dipoles that will assume some ordering during the static DFT calculation and can induce a large electric field when misoriented or form domains.^{74,75} Under ambient conditions, the fast thermal motion of molecules averages out dipole orientations,⁵¹ which is effectively represented in the static model by a large spherical cation such as cesium. After relaxing the surface structure, we observed a surface reconstruction that mainly consists of attraction of Cs atoms at the surface layer toward the slab center by ca. 0.8 Å.

The lowest band gap of 0.5 eV for the cubic slab model with SOC occurs at $\mathbf{k} = (1/2, 1/2, 0)$, which is expected due to the zone folding and the odd multiplier (3) used in the

construction of the supercell in the lateral direction. The bulk band gap is only 0.2 eV with SOC, which is extremely underestimated relative to the experimental low-temperature band gap of $E_g = 1.72$ eV for cubic CsPbI_3 .⁷⁶ This shortcoming is usual for DFT-PBE with SOC and this material system. The prior study²⁹ of $n = 5$ Ruddlesden–Popper phase $[\text{CH}_3(\text{CH}_2)_3\text{NH}_3]_2(\text{CH}_3\text{NH}_3)_4\text{Pb}_3\text{I}_{16}$ also reported a low band gap $E_g \approx 0.3$ eV (DFT-PBE with SOC). Prior calculation⁴⁹ of cubic CsPbI_3 bulk quoted $E_g \approx 0.5$ eV (DFT-PBE with SOC) versus $E_g \approx 1.6$ eV (quasiparticle GW with SOC). The large size of our supercells for studying defects precludes calculations at higher levels of theory (e.g., hybrid functionals or quasiparticle GW) to correct for the band gap error. The band gap error of DFT–PBE can be largely recovered when SOC is omitted as a result of the error cancellation⁷⁷ ($E_g = 1.3$ eV in bulk and $E_g = 1.4$ eV in slab). Later we will find this correction essential when calculating the formation energy of n -type defects with energy levels close to the CBE. Increase of the band gap for the slab model versus bulk can be attributed to a quantum confinement effect.

Since transport of charge carriers occurs at band edges, it is interesting to explore the spatial distribution of states associated with VBE and CBE in the model with the surface. Figure 1b,c shows atom-resolved $|\psi(r)|^2$ for these two states derived from the VASP PROCAR file generated in a calculation with SOC for the cubic structure (data for the tetragonal phase are shown in Figure S1). The VBE state is confined closer to the center of the slab, while the CBE state is distributed more evenly throughout the slab thickness. Notably, band edge states are not localized at the surface in the calculation with

SOC, which implies that the surface does not act as a trap for free carriers (see the effective band diagram in the inset of Figure 1c). This result is in line with the earlier findings of Buin et al.;²⁶ it is also backed up by calculations at the HSE06 level of theory (see the Supporting Information Section, Figure S2a,b) to ensure that this is not an artifact of the PBE underestimated band gap. The tetragonal structure favors an even stronger repulsion of holes from the surface but also a weak attraction of electrons to the surface (see Figure S1).

Our results for $|\psi(r)|^2$ in Figure 1b,c are similar to the results of Haruyama et al.²⁷ for MAPbI₃(100) PbI-terminated surface with SOC. However, they are qualitatively different from those by Stoumpos et al.,²⁹ who found VBE and CBE states of a Ruddlesden-Popper bulk phase ($\text{CH}_3(\text{CH}_2)_3\text{NH}_3)_2(\text{CH}_3\text{NH}_3)_4\text{Pb}_5\text{I}_{16}$ ($n = 5$) being confined near the surface. The difference can be attributed (presumably) to peculiarities in the static arrangement of MA dipoles having mirror symmetry with respect to the slab center. This could have created a zigzag potential causing spatial separation between VBE and CBE states as in ref 75. Our structure does not have those polar molecules and should give results relevant to ambient conditions (see the argument presented above about thermal motion). Experimental data of Dymshits et al.⁷⁸ and Kim et al.⁷⁹ give two contradictory pictures of the band bending at the (100) surface of MAPbI₃.

In the calculation without SOC, the spatial distribution of the CBE state slightly changed its behavior toward attraction to the surface, while the VBE state (not affected by SOC) remains unchanged (see Figure S3a,b). Data presented by Meggiolaro et al.²⁸ show the same behavior without SOC for the (100) surface of MAI-terminated MAPbI₃. Haruyama et al.²⁷ also noted the same qualitative difference between lowest unoccupied orbitals calculated with and without SOC for the (100) PbI-terminated surface of MAPbI₃. This observation suggests that the nonrelativistic electronic structure shows less tolerance to surface states. (Brandt et al.¹² also noted the essential role of SOC in the defect tolerance of bulk lead-halide perovskites.). To explain this observation, we recall that the CBE in lead-halide perovskites corresponds to a Pb-p_{1/2} split-off band in the presence of SOC,⁷⁷ where Pb-p_{x,y,z} orbitals should be mixed in nearly equal proportions by the SOC Hamiltonian. The orbital composition of the CBE state of our slab model confirms that expectation

$$|\psi_{\text{CBE}}|^2 = 0.31 |\text{p}_{x,\text{Pb}}|^2 + 0.31 |\text{p}_{y,\text{Pb}}|^2 + \mathbf{0.16} |\text{p}_{z,\text{Pb}}|^2 \\ + \dots \text{ (with SOC)}$$

The p_z orbital is affected by the quantum confinement of the slab, and we would anticipate it to dominate in the center of the slab following analogy with the “particle in a box” problem. However, the orbital mixing is not required without SOC, thus the CBE state comprises only Pb-p_{x,y} orbitals

$$|\psi_{\text{CBE}}|^2 = 0.40 |\text{p}_{x,\text{Pb}}|^2 + 0.40 |\text{p}_{y,\text{Pb}}|^2 + \mathbf{0} |\text{p}_{z,\text{Pb}}|^2 \\ + \dots \text{ (without SOC)}$$

that are not subjected to confinement in the lateral plane of the slab; the Pb-p_z states are decoupled from Pb-p_{x,y} states and moved to higher energies within the conduction band and assume the shape expected from the quantum confinement.

To elucidate the role of surface reconstruction, we performed a similar analysis of VBE and CBE states on a

model without the relaxation of atomic positions (see Figure S3c,d). The $|\psi(r)|^2$ envelope function profiles for both band edges are nearly identical and closely resemble a “particle in a box” solution. Thus, the surface reconstruction creates an additional electric field pointing from the surface into the slab that shapes VBE/CBE states, causing an additional repulsion/atraction of $|\psi(r)|^2$ from/to the surface. It should be noted that details of the surface reconstruction are specific to the cation (Cs in this case). The magnitude and direction of the electric field can be influenced by the size of molecules at the surface and the presence of a dipole moment within the molecule.²⁴

Formation Energy of Neutral Defects. Here, we will calculate the formation energy of native vacancies according to eq 1 to determine the propensity of their occurrence at the surface versus bulk. The formation energy depends on the chemical potential of elements in a reservoir, which is generally expressed as

$$\mu = \mu^\circ + \Delta\mu \quad (5)$$

where μ° is the chemical potential of an element under standard thermodynamic conditions, and $\Delta\mu$ captures any deviations from the standard conditions. For solid elements, it is sufficient to approximate μ° by using the DFT total energy E_{tot} of their most stable polymorph.⁵⁹ The chemical potential adjustment ($\Delta\mu$) reflects the chemical activity of elements under a specific synthesis environment and obeys restrictions imposed by the thermodynamic stability of solid phases,⁶¹ as well as additional constraints due to the presence of reactants as ions in solution

$$\Delta\mu(\text{Cs}) + \Delta\mu(\text{Pb}) + 3\Delta\mu(\text{I}) \geq \Delta H_f(\text{CsPbI}_3) \quad (6a)$$

$$\Delta\mu(\text{Cs}) + \Delta\mu(\text{I}) < \Delta H_f(\text{CsI}) \quad (6b)$$

$$\Delta\mu(\text{Pb}) + 2\Delta\mu(\text{I}) < \Delta H_f(\text{PbI}_2) \quad (6c)$$

$$\Delta\mu(\text{Cs}) \leq \Delta G^\circ(\text{Cs}^+, \text{aq}) \quad (6d)$$

$$\Delta\mu(\text{Pb}) \leq \Delta G^\circ(\text{Pb}^{2+}, \text{aq}) \quad (6e)$$

$$\Delta\mu(\text{I}) \leq \Delta G^\circ(\text{I}^-, \text{aq}) \quad (6f)$$

The formation free energy of a solid is approximated by the enthalpy (ΔH_f) at 0 K in our calculations. It can be noted that the final temperature correction is computationally very expensive, while its effect on the formation enthalpy of solids is much smaller than the chemical accuracy of DFT-PBE.⁸⁰

Table 1 summarizes the DFT formation enthalpies of relevant solids compared to the experiment to show the chemical accuracy of our calculations. The largest error is about 0.2 eV per atom. The effect of SOC is notable for lead-

Table 1. Formation Enthalpies of Solids ΔH_f (eV/f.u.)

method	CsI ($Pm\bar{3}m$, 221)	PbI ₂ ($R\bar{3}m$, 166)	$\delta\text{-CsPbI}_3$ ($Pnma$, 62)
PBE + D3 without SOC	-3.23	-1.96	-5.44
PBE + D3 with SOC	-3.20	-1.79	-5.23
HSE06 without SOC	-3.31	-2.16	-5.66
HSE06 with SOC	-3.29	-1.98	-5.46
experiment	-3.61 ⁸²	-1.81 ⁸³	-5.60 ^a

^aEstimated based on the experimental enthalpy of -0.18 eV/f.u. for the reaction CsI + PbI₂ → CsPbI₃ (ref 84).

containing structures without a clear trend on whether the relativistic effects improve or not the agreement with the experiment. The values of $\Delta\mu$ were tailored to the activity of ionic species in an aqueous solution. From the Pourbaix atlas,⁸¹ we find $\Delta G^\circ(\text{Cs}^+, \text{aq}) = -2.92 \text{ eV}$, $\Delta G^\circ(\text{Pb}^{2+}, \text{aq}) = -0.25 \text{ eV}$, and $\Delta G^\circ(\text{I}^-, \text{aq}) = -0.54 \text{ eV}$.

Figure 2 illustrates the region of chemical potentials corresponding to the stability of the perovskite phase. At the

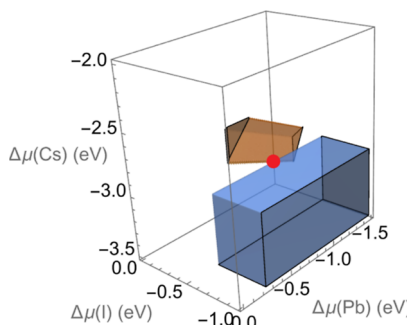


Figure 2. Region of CsPbI_3 thermodynamic stability (brown, based on DFT data without SOC) that satisfies eqs 6a–6c and the region of chemical potentials of ions accessible in an aqueous environment (blue) that satisfies eqs 6d–6f. The red dot represents the point of overlap between the two regions.

same time, we need to acknowledge that the energy of dissolved species is additionally lowered relative to their bulk phase by $\Delta\mu$: the more soluble the ion is, the lower $\Delta\mu$ is (e.g., Cs^+). Conditions that favor CsPbI_3 precipitation from the solution (red point in **Figure 2**) allow us to fix $\Delta\mu$

$$\Delta\mu(\text{Cs}) \approx \Delta G^\circ(\text{Cs}^+, \text{aq}) \quad (7a)$$

$$\Delta\mu(\text{I}) \approx \Delta G^\circ(\text{I}^-, \text{aq}) \quad (7b)$$

$$\begin{aligned} \Delta H_f(\text{CsPbI}_3) - \Delta G^\circ(\text{Cs}^+, \text{aq}) - \dots \\ \dots 3\Delta G^\circ(\text{I}^-, \text{aq}) \leq \Delta\mu(\text{Pb}) \leq \Delta H_f(\text{PbI}_2) \\ - 2\Delta G^\circ(\text{I}^-, \text{aq}). \end{aligned} \quad (7c)$$

Results for the chemical potentials are summarized in **Table 2**. The standard conditions at which ΔG° 's are derived assume a 1 M concentration of aqueous species, while the chemical potentials can be additionally adjusted in case of significant deviations from that (see p. 5–113 in ref 85). We have two sets of chemical potentials: with and without SOC. The effect

Table 2. Chemical Potentials of Elements That Fulfill Constraints (7) Relevant to Solution-Processed Synthesis^b

element	without SOC		with SOC	
	$\Delta\mu$ (eV)	μ (eV)	$\Delta\mu$ (eV)	μ (eV)
PBE + D3				
Cs	-2.92	-3.909	-2.92	-4.050
Pb	-0.89	-4.724	-0.70 ^a	-5.044
I	-0.54	-2.252	-0.54	-2.409
HSE06				
Cs	-2.92	-3.911	-2.92	-4.048
Pb	-1.10	-5.238	-0.91	-5.535
I	-0.54	-2.587	-0.54	-2.732

^aThe constraint (7c) is satisfied with a small error of 0.02 eV. ^bTwo sets of data represent different levels of theory: PBE + D3 and HSE06.

of SOC on the chemical potential is largest for lead as it is the heaviest element.

Our approach to finding the chemical potentials augments the common practice,¹⁰ which involves defining a region of chemical potentials in which MAPbI_3 is stable, while MAI and PbI_2 are not (the brown region in **Figure 2**), and selecting two extreme sets of chemical potentials (referred to as I-rich/Pb-poor and I-poor/Pb-rich sets) from the multitude of possibilities.⁹ The resultant defect formation energies typically varied by 1–3 eV, depending on which extreme set of chemical potentials is selected,^{10,15,33} which is the largest source of uncertainty in the calculation of E_d .

Now we present results for the formation energy of neutral defects at the surface versus bulk calculated with and without SOC in the cubic structure (large model size) in **Table 3**. There are several notable points: (i) the surface favors the formation of Cs vacancies. (ii) Lead vacancies are more favorable in the bulk than at the surface. (iii) The formation energies of iodine and lead vacancies are reduced after adding SOC. The SOC renormalization of the V_{I} defect formation energy can be attributed to the band gap error (see **Figure S4**). The iodine vacancy creates an *n*-type defect with one electron promoted to the conduction band. The energy penalty is less when the band gap is underestimated. Thus, the E_d results at the PBE level without SOC are more reliable for V_{I} (see **Table 3**) and for other *n*-type defects, in general. However, we should not expect the band gap error to explain the SOC renormalization of the V_{Pb} defect formation energy. The lead vacancy removes two electrons from the valence band, the energy position of which is not much affected by SOC. In this case, the renormalization is due to the lower chemical potential of lead with SOC (**Table 2**). Thus, the results with SOC are more trustworthy for V_{Pb} . The higher energy of the Pb vacancy at the surface can be explained by the very unfavorable position of the iodine atom immediately above the vacancy at the surface, which is nearly detached (see **Figure S5b**). We tried removing this iodine atom to create a *p*-type V_{PbI} divacancy at the surface (see **Figure S5d**). Its formation energy in the neutral state comes second lowest at the surface after V_{Cs} suggesting that the lead–iodine divacancy is more plausible at the surface than the lead vacancy alone. A lower energy of V_{Cs} at the surface can be connected with a higher Madelung energy of the surface site facing a vacuum and the purely ionic nature of the $\text{Cs}-\text{PbI}_3$ bond.

Next, we discuss similarities and differences in the formation energy of neutral vacancies in the tetragonal versus cubic structure of CsPbI_3 (**Table 3**). The tetragonality of CsPbI_3 is close to that of MAPbI_3 at about 150–200 K.⁵² At the surface, the defect formation energies of cesium and lead vacancies are not sensitive (within 0.1 eV) to the choice of the phase. The iodine vacancy shows about 0.3 eV greater formation energy in the tetragonal phase, which is largely due to the greater band gap of the tetragonal phase (see **Figure S4**). The net difference in $E_d(V_{\text{I}}^0)$ between the tetragonal structure and the cubic phase (excluding the effect of the band gap) is only 0.1 eV. Thus, the formation energies of surface vacancies calculated using the cubic phase also apply to the tetragonal structure. In bulk, the above discussion applies to cesium and iodine vacancies. The formation energy of a lead vacancy indeed shows a greater disparity of ca. 0.3 eV between the cubic and tetragonal structures. To rule out a possible nonphysical structure relaxation⁸⁶ due to dynamical instability of the cubic structure, we placed the Pb atom back into the relaxed

Table 3. Formation Energy (eV) of Neutral Vacancies in CsPbI_3 Calculated at the Surface of a Slab Model and in Bulk at Two Levels of Theory (HSE06 and PBE + D3) and Varying Sizes of the Model for Cubic and Tetragonal Phases^d

location	model size	phase	XC approx.	V_{Cs}	V_{I}	V_{Pb}	V_{PbI}
slab, surf.	$3 \times 3 \times 6$	cubic	PBE + D3	0.40/0.22	1.7/0.88	1.4/1.2	0.85/0.75
	$2\sqrt{2} \times 2\sqrt{2} \times 5$	tetragonal	PBE + D3	0.48/0.29	2.0/1.2	1.5/1.2	0.88/0.74
	$2 \times 2 \times 3$	cubic	PBE + D3	0.54/0.36	1.8/1.1	1.7/1.5	
	$2 \times 2 \times 3$	cubic	HSE06	0.61/0.44	1.9/1.2	2.2/1.9	
	$4 \times 4 \times 4$	cubic	PBE + D3	0.91/0.74	1.6/0.62	0.94/0.69	
	$3\sqrt{2} \times 3\sqrt{2} \times 4$	tetragonal	PBE + D3	0.95 ^a /0.77	1.7 ^b /0.90	1.3 ^c /1.0	

^aOther calculations for MAPbI_3 and CsPbI_3 including adjustment for differences in the chemical potentials of elements: 0.77,¹⁰ 0.05³³ eV. ^b1.3,¹⁰ 0.96³³ eV. ^c1.8,¹⁰ 0.90³³ eV. ^dThe numerator/denominator corresponds to the results obtained without/with SOC.

Table 4. Thermodynamic Transition Energy Levels (eV) Associated with Vacancies in Cubic and Tetragonal CsPbI_3 ^f

structure	state	surface		bulk	
		without SOC	with SOC	without SOC	with SOC
cubic	host^{+0}	$E_{\text{VBE}} + 0.08$	$E_{\text{VBE}} + 0.07^a$	$E_{\text{VBE}} + 0.01$	$E_{\text{VBE}} + 0.01$
	$\text{host}^{0/-}$	$E_{\text{CBE}} - 0.07$	$E_{\text{CBE}} - 0.07^b$	$E_{\text{CBE}} - 0.01$	$E_{\text{CBE}} - 0.01$
	$V_{\text{Cs}}^{0/-}$	$E_{\text{VBE}} - 0.02$	$E_{\text{VBE}} - 0.05^c$	$E_{\text{VBE}} + 0$	$E_{\text{VBE}} + 0$
	$V_{\text{I}}^{+/0}$	$E_{\text{CBE}} - 0.02$	$E_{\text{CBE}} + 0.07^d$	$E_{\text{CBE}} - 0.03$	$E_{\text{CBE}} + 0.02$
	$V_{\text{Pb}}^{0/2-}$		$E_{\text{VBE}} + 0^e$	$E_{\text{VBE}} + 0$	$E_{\text{VBE}} + 0$
	$V_{\text{Pb}}^{0/-}$	$E_{\text{VBE}} + 0.06$			
	$V_{\text{Pb}}^{-2/-}$	$E_{\text{VBE}} + 0.08$			
	$V_{\text{Pbi}}^{0/-}$	$E_{\text{VBE}} - 0.01$	$E_{\text{VBE}} - 0.04$		
	host^{+0}	$E_{\text{VBE}} + 0.02$	$E_{\text{VBE}} + 0.01$	$E_{\text{VBE}} + 0.01$	$E_{\text{VBE}} + 0.01$
	$\text{host}^{0/-}$	$E_{\text{CBE}} - 0.07$	$E_{\text{CBE}} - 0.05$	$E_{\text{CBE}} - 0.01$	$E_{\text{CBE}} - 0.01$
tetragonal	$V_{\text{Cs}}^{0/-}$	$E_{\text{VBE}} + 0.08$	$E_{\text{VBE}} + 0.05$	$E_{\text{VBE}} + 0$	$E_{\text{VBE}} + 0$
	$V_{\text{I}}^{+/0}$	$E_{\text{CBE}} - 0.19$	$E_{\text{CBE}} - 0.04$	$E_{\text{CBE}} + 0$	$E_{\text{CBE}} + 0$
	$V_{\text{Pb}}^{0/2-}$		$E_{\text{VBE}} + 0.07$	$E_{\text{VBE}} - 0.01$	$E_{\text{VBE}} + 0$
	$V_{\text{Pb}}^{0/-}$	$E_{\text{VBE}} + 0.07$			
	$V_{\text{Pb}}^{-2/-}$	$E_{\text{VBE}} + 0.48$	$E_{\text{VBE}} + 0.36$		
	$V_{\text{Pbi}}^{0/-}$	$E_{\text{VBE}} + 0.11$	$E_{\text{VBE}} + 0.06$		

^aTransition energy levels evaluated at the HSE06 with SOC level of theory for slab model size of $2 \times 2 \times 3$, cubic phase: $E_{\text{VBE}} + 0.11$. ^b $E_{\text{CBE}} - 0.20$.

^c $E_{\text{VBE}} - 0.09$. ^d $E_{\text{CBE}} + 0.05$. ^e $E_{\text{VBE}} + 0.02$. ^fTransition levels of the host without defects indicate the positions of perceived band edges. Energies of acceptor/donor-like states are given relative to Kohn–Sham VBE/CBE eigenvalues.

structure with the vacancy and were able to recover (after subsequent structural relaxation) the total energy of the defect-free structure within 1 meV.

In order to assess the sensitivity of defect formation energies to the selection of XC functional, we performed additional calculations using a hybrid functional HSE06 with and without SOC. Due to the computational intensity of HSE06, we had to use a smaller slab model ($2 \times 2 \times 3$). Results for the formation energy of neutral vacancies at the surface are given in Table 3. We also obtained PBE + D3 results for the same model size to facilitate the comparison. The formation energies of a cesium surface vacancy are identical between PBE + D3 and HSE06 within 0.1 eV. The formation energy of a neutral surface iodine vacancy also seems to be identical between PBE + D3 and HSE06, but a more careful analysis taking into account its sensitivity to the calculated band gap (see Figure S4) shows $E_d(V_{\text{I}}^0)$ being 0.2–0.3 eV lower at the HSE06 level of theory for the same band gap. Taking into account the limited model size effect and the correct experimental band gap of about 1.5 eV, we can estimate $E_d(V_{\text{I}}^0) \approx 1.5$ eV. The formation energies of neutral lead vacancies differ more significantly (by 0.4–0.5 eV) between HSE06 and PBE + D3, making this defect even more unlikely at the surface.

For the sake of completeness, we list the calculated formation energies of vacancies in lead-halide perovskites available in the literature. However, the data scattering is too

large to draw any conclusions. The footnotes of Table 3 contain data for bulk MAPbI_3 that can be directly compared with our results, since the authors^{10,33} reported the chemical potentials, and we were able to adjust for the differences with our choice. Other data in the literature show even more variability in the formation energies of neutral vacancies due to a wide range of chemical potentials. Li et al.¹⁵ reported the energies for CsPbI_3 : $E_d(V_{\text{Cs}}) = 1.3 \dots 0.3$ eV, $E_d(V_{\text{I}}) = -0.2 \dots 0.8$ eV, $E_d(V_{\text{Pb}}) = 0.4 \dots -1.5$ eV (the range is from lead-rich to lead-poor conditions). The data from Buin et al.²⁶ for defects in bulk MAPbI_3 are $E_d(V_{\text{MA}}) = 1.8 \dots 0.7$ eV, $E_d(V_{\text{I}}) = 0.7 \dots 1.7$ eV, $E_d(V_{\text{Pb}}) = 2.7 \dots 0.6$ eV.

Charged Defects and Transition Energy Levels. We assess the position of the energy levels associated with defects relative to the band edges of the defect-free slab model using a transition energy level technique. The goal of this analysis is to find out if electronic states associated with vacancies at the surface of lead-halide perovskites emerge in the band gap (especially deep levels) as those will have an adverse effect on transport properties and can serve as nonradiative recombination centers. As a reference, it is useful to establish the energy levels associated with the creation of an electron or a hole in the defect-free structure, as previously suggested by Hellström et al.⁸⁷ Following eq 4, the corresponding energy levels are⁶¹

$$\mu_{e,v} \equiv \epsilon(\text{host}^{+/0}) = E_{\text{tot}}(\text{host}) - E_{\text{tot}}^*(\text{host}^+) \quad (8a)$$

$$\mu_{e,c} \equiv \epsilon(\text{host}^{0/-}) = E_{\text{tot}}^*(\text{host}^-) - E_{\text{tot}}(\text{host}) \quad (8b)$$

Here, the asterisk (*) implies that the DFT total energy of a charged cell includes the correction term E_{corr} in eq 1. The total energy difference between the neutral and charged model ($\pm 1e$) is related to the first ionization potential and the electron affinity.^{88–90} For extended states in the dilute limit of hole/electron concentration, $\mu_{e,v/c}$ approaches the Kohn–Sham VBE/CBE eigenenergies,⁶¹ respectively. Data in Table 4 show nearly perfect agreement between $\epsilon(\text{host}^{\pm/0})$ states and the band edges in the bulk, which indicates the efficiency of corrections to the total energy of charged bulk cells (with the band filling correction being dominant in this case). Without corrections, those levels would be located 0.1–0.2 eV away from the band edges, delving into the valence or conduction band. Gerstmann et al.⁹¹ also noted that the Makov–Payne⁶² monopole term cancels out in the limit of delocalized states.

The agreement between the band edges and the $\epsilon(\text{host}^{\pm/0})$ transition energy levels is less favorable for the slab model (Table 4). Taking the $\epsilon(\text{host}^{0/-})$ level in the tetragonal slab without SOC as an example, we find from uncorrected total energies $\mu_{e,c} = E_{\text{CBE}} + 0.06$ eV. The potential alignment (−0.08 eV) and the band filling (−0.04 eV) corrections bring the energy level at $\mu_{e,v} = E_{\text{CBE}} - 0.07$ eV indicating some overcorrection in the slab model. We performed additional checks and ruled out the k -mesh density and the structure relaxation (vertical vs nonvertical transitions) as possible causes for the 0.07 eV discrepancy. Thus, the remaining misalignment between $\mu_{e,v/c}$ and VBE/CBE indicates the magnitude of ambiguity that can still be present in the analysis of the defect energy levels of the slab model.

An energy correction $\delta U(q)$ associated with the spurious electrostatic energy of charged stacked slabs^{5,64–67} was evaluated to determine its ability to explain the slight discrepancy between the electron chemical potential $\mu_{e,v/c}$ and VBE/CBE. In the Supporting Information, we provided details on the calculation of the U_{per} for the defect-free tetragonal slab with a charge of $q = \pm 1$ (see Figures S9 and S10). The electrostatic potential energy of defect-free charged stacked slabs is approximately 0.06 eV, regardless of the sign of q . Subtracting this energy from the total energy of the charged slabs $E_{\text{tot}}^*(\text{host}^{\pm})$ effectively stabilizes the charged state and shifts the transition energy levels $\epsilon(\text{host}^{+/0})$ and $\epsilon(\text{host}^{0/-})$ further away from the band edges into the band gap by 0.06 eV enhancing the discrepancy between $\mu_{e,v/c}$ and VBE/CBE eigenvalues. It is worth noting that the electrostatic correction in the literature^{5,64–67} has always been tested for localized defect states. Komsa et al.⁶⁸ expressed reservations about the applicability of “simple electrostatics” in cases where charge delocalization is observed, as in our case of extended VBE and CBE states. Therefore, the electrostatic correction is not included in Table 4, however its effect can be inferred from Figure S11 (see the Supporting Information Section) where we presented both corrected and uncorrected transition energy levels for vacancies in slabs of the tetragonal structure.

Table 4 summarizes transition energy levels for vacancies at the surface, calculated with and without SOC. These values reflect *thermodynamic* energy levels, which implies that they include relaxation of the structures in all charged states.^{92,93} All bulk states are shallow, and their energy positions are given relative to the VBE or CBE energy eigenvalues for p - and n -

type defects, respectively. Most defect energy levels at the surface remain close to the band edges and do not form detrimental deep traps within the band gap, indicating that the tolerance of the electronic structure of lead-halide perovskites to defects also extends to the surface. This conclusion is robust with respect to selection of the XC functional (see HSE06 data in the footnotes of Table 4) and supports prior studies by Song et al.³³ and Perez et al.³¹ based on thinner slab models. The only exception is the deep $\epsilon(V_{\text{Pb}}^{-1/2-})$ transition energy level at the surface of the tetragonal phase. However, the formation energies (Table 3) suggest that lead–iodine divacancies are significantly more prevalent than lead-only vacancies.

Our data in Table 4 show that the transition energy levels of vacancies are shallow with SOC and remain the same without SOC. This is different from the statement by Brandt et al.,¹² suggesting that the vacancy-type defects in MAPbI_3 are resonant with the band edges due to relativistic effects shifting the CBE down in energy. We observe that the $V_1^{+/0}$ energy level shifts up relative to the CBE in both slab and bulk models, but the magnitude (0.05–0.09 eV) is very small in comparison to the band gap renormalization due to SOC. Lany and Zunger⁶⁰ noted that this type of defects falls into the category of delocalized host states perturbed by a screened Coulomb potential of a defect, resulting in a shallow energy level that moves together with the associated band edge when the gap changes, for example, when adding SOC or using a high-level theory to circumvent the DFT band gap problem. Hence, the energy levels follow the band edges as the band gap opens significantly in calculations without SOC. The more delocalized nature of the $V_1^{+/0}$ state with SOC (similar to the discussion on surface states and driven by the $\text{Pb}-\text{p}_{x,y,z}$ orbital mixing) explains the shallower energy position of the states in both slab and bulk models. (A more quantitative discussion of localization follows in the next subsection.) If we take into account the electrostatic potential energy for charged periodic slabs (see the Supporting Information section for details), the transition energy levels will shift even closer to the band edges (Figure S11), reinforcing the shallow nature of charge transition energy level associated with vacancies at the surface.

It should be noted that the energy position of transition levels in lead-halide perovskites is much better reproducible across the literature^{8–10,16,26} than the formation energy of defects. The only notable outliers are the work by Du¹¹ and by Meggiolaro et al.¹⁶ Du¹¹ found that energy levels of host-like states, such as $\epsilon(V_1^{+/0})$, do not follow the band edges as if they were localized deep-level states. Meggiolaro et al.¹⁶ obtained midgap states for V_{Pb} in bulk.

Having calculated the transition energy levels and the formation energy of neutral defects, it is possible to visualize the formation energy of charged defects with respect to the Fermi energy. The results for the cubic phase are presented in Figure 3. Since the data for the tetragonal phase are very similar (see the Supporting Information section, Figure S11), we will focus the discussion on the cubic phase in the remaining part of the paper. In bulk, the Fermi energy is pinned slightly above the VBE, which is consistent with the intrinsic or weak p -type character of lead-halide perovskites.^{24,78,94,95} Predominant vacancies in the bulk are V_{Pb}^{2-} and V_1^+ . (Yin et al.¹⁰ previously identified V_{Pb} as a dominant p -type defect in bulk based on DFT calculations.). At the surface, our results suggest pinning of the Fermi energy at the VBE and segregation of V_{Cs}^- and V_1^+ vacancies. The ratio $[V_{\text{Cs}}^-]/[V_1^+]$ between the concentration of Cs and I vacancies will

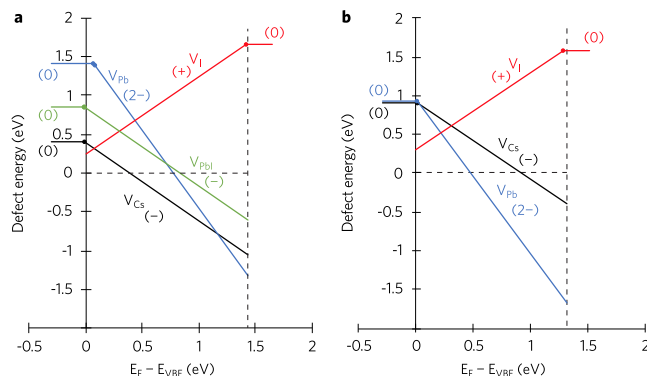


Figure 3. Formation energy of vacancies at the surface (a) and in the bulk (b) of cubic CsPbI_3 as a function of the Fermi energy (E_F). Values in brackets represent the charge state. The vertical dashed lines mark the location of the CBE. The chemical potential of elements is tuned to reflect solution-processed synthesis conditions. Results are shown without SOC to compensate for the DFT band gap error. All defect energies associated with the lead vacancy should be adjusted by ca. 0.2 eV (shifted down) to compensate for the overestimation of its chemical potential due to the omission of SOC.

determine the negative/positive charge of the surface. The calculated formation energies of the V_{Cs}^- and V_I^+ vacancies at

the surface are very close in the *p*-type region (Figure 3a). Thus, any subtle changes in the chemical potential of these two species can shift the balance. The experimental study of Kim et al.⁷⁹ supports the dominance of iodine vacancies at the (100) surface of MAPbI_3 . Figure S11 in the Supporting Information section shows the effect of the periodic slab electrostatic correction on the formation energy of charged defects using the tetragonal phase as an example. This correction does not change the overall trend.

So far, we have discussed the thermodynamic transition energy levels. When nonradiative transitions occur through deep energy levels, atomic positions do not have time to relax during the fast electronic transition (e.g., the capture of an electron from the CBE by a deep trap). As a result, the thermodynamic and optical transition levels will differ by the value of a Franck–Condon shift, which can be as high as 0.5 eV for a carbon deep acceptor $\text{C}_N^{0/-}$ in GaN.⁹² Signature of a large Franck–Condon shift would be a significant change in the DFT total energy of the defect model, which occurs during structural relaxation in a charged state when starting from a *fully relaxed* geometry of the neutral defect, indicating a large Franck–Condon shift. To assess the total energy of charged states without additional structural relaxation, we performed calculations of transition energy levels of defects using the fully

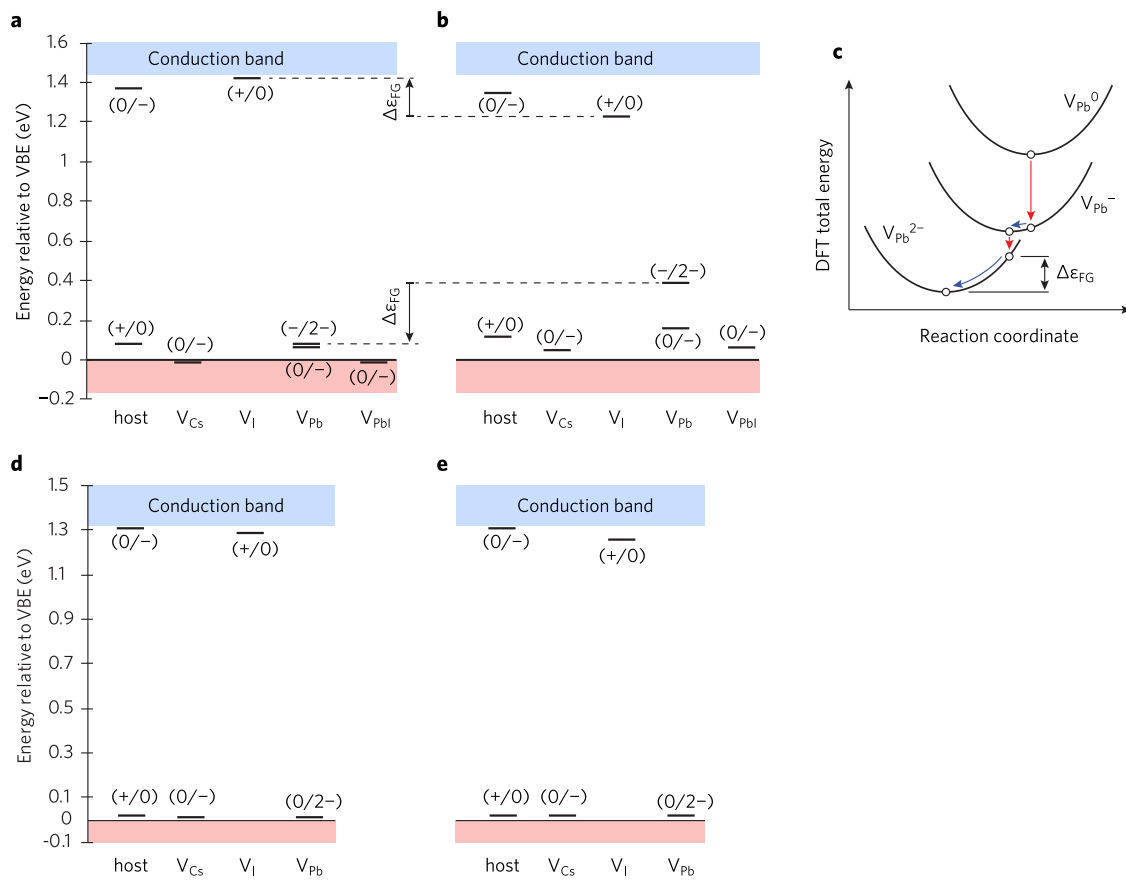


Figure 4. Transition energy levels for vacancies in cubic CsPbI_3 at the surface (a,b) and in the bulk (d,e). Transition levels of the host without defects indicate the position of the perceived band edges. The energy levels are shown in a thermodynamic limit (a,d), meaning unconstrained reaction coordinates, and also constrained to vertical transitions (b,e). Values in brackets indicate the charge state. The configuration energy diagram (c) schematically shows the evolution of the DFT total energy of the Pb surface vacancy at different charge states as a function of a reaction coordinate (atomic positions). Red arrows represent vertical electronic transitions, while blue arrows correspond to nonradiative energy dissipation processes. $\Delta\epsilon_{FG}$ indicates a Franck–Condon shift, which is most prominent for the transition energy levels $\epsilon(V_{\text{Pb}}^{-2-})$ and $\epsilon(V_I^{+0})$ at the surface. The results are shown without SOC to compensate for the DFT band gap error.

relaxed geometry in the neutral state and compared the results to those when additional structural relaxation was included (Figure 4). In bulk, there are no major differences between transition energy levels calculated with and without relaxation of charged states. However, two energy levels ($V_{\text{pb}}^{-2/-}$ and $V_1^{+/-}$) stand out from the others when they are calculated at the surface. The thermodynamic energy level of the shallow acceptor $V_{\text{pb}}^{-2/-}$ becomes a *deep* acceptor for optical electronic transitions, likely due to the loosely bound iodine at the surface (see Figure S5b). The configuration energy diagram (Figure 4c) illustrates transitions between successive charge states, involving electronic transitions and nonradiative energy dissipation. It can be speculated that defects with a large Franck–Condon shift are likely to become centers of nonradiative recombination. However, it should be noted that the formation energy of the alternative V_{pbI} divacancy at the surface is lower than that of V_{pb} in the *p*-type region (Figure 3). The energy level $\epsilon(V_{\text{pbI}}^{0/-})$ is shallow and the Franck–Condon shift is rather small (Figure 4) making V_{pbI} divacancy not a deep trap.

Localization of Defect States. The wave function PR is employed to quantify changes in its localization at the band edges. The PR of an eigenstate with the energy $E_{n,k}$ is defined as^{96,97}

$$\text{PR}(E_{n,k}) = \frac{\left(\sum_{\alpha=1}^N |\psi_{n,k,\alpha}|^2\right)^2}{\sum_{\alpha=1}^N |\psi_{n,k,\alpha}|^4} \quad (9)$$

where $|\psi_{n,k,\alpha}|^2$ is the probability of finding an electron of the specific eigenstate within a sphere centered at the atomic site α . The summation index α runs over all the atomic sites N . The surface slab model has 288 atoms (63-Cs, 54-Pb, and 171-I), and the bulk model has 320 atoms (64-Cs, 64-Pb, and 192-I). The PR has two extremes: (i) PR = N when the wave function is fully delocalized (i.e., uniformly distributed among all N atoms) and (ii) PR = 1 if the wave function is localized on only one of the atoms. Since Cs atoms do not contribute to electronic states at the band edges of lead-halide perovskites, the upper limit of PR will effectively become 226 and 256 for the slab and bulk models, respectively.

In defect-free structures, the VBE has a higher PR compared with CBE (Table 5). The PR of bulk VBE is nearly identical to the number of Pb and I atoms in the model. This result can be explained by a nearly equal participation of both lead and iodine atoms in the VBE state (Figure 1b), while the CBE is dominated by lead with only a weak presence of iodine (Figure

Table 5. Localization of Electronic States at the Band Edges of Cubic CsPbI_3 with Defects Assessed by PR^a

defect	surface slab ($N = 288$)		bulk ($N = 320$)	
	without SOC	with SOC	without SOC	with SOC
no defect (ref.)	129/65	141/85	240/98	246/90
V_{Cs}	<u>131/31</u>	<u>142/71</u>	<u>236/96</u>	<u>242/91</u>
V_{pb}	<u>122/30</u>	<u>136/67</u>	<u>234/88</u>	<u>240/88</u>
V_1	125/ <u>46</u>	116/ <u>67</u>	233/ <u>55</u>	234/ <u>91</u>
V_{pbI}	<u>122/29</u>	<u>135/69</u>		

^aValues significantly lower than the reference without defects indicate localization. Values in the numerator/denominator refer to VBE/CBE states. The PR of the VBE state is underlined for *p*-type defects, and the CBE state is underlined for *n*-type. N is the total number of atoms in each model without defects.

1c). The PR is reduced by 35% in the slab VBE, which is subject to a combined effect of quantum confinement and an electric field due to surface reconstruction. The PR of CBE states in the bulk and slab with SOC is nearly identical, taking into account the different number of atoms in the two models. This is ascribed to the quantum confinement and electric field opposing each other. The delocalization due to SOC (higher PR) is noted in the defect-free slab model but not in the bulk, suggesting that SOC is an essential ingredient for a proper description of the spatial distribution of surface states.

The *p*-type vacancies (V_{Cs} , V_{pb} , and V_{pbI}) leave the PR of the VBE almost unchanged in the slab and in the bulk models (see Table 5 as well as Figures S6a,b,d and S7a,b,d for the spatial distribution of $|\psi_{\text{VBE}}(\mathbf{r})|^2$ in cubic and tetragonal models, respectively). The *n*-type defect (V_1) exhibits stronger localization of the CBE state when SOC is omitted, while the PR of the CBE is recovered back to the defect-free level with SOC in the cubic structure (see Figure S6c), indicating its importance for a proper description of the spatial distribution of states associated with *n*-type defects. In the tetragonal phase with the iodine vacancy at the surface, the CBE states remain confined at the surface despite SOC (Figure S7c); it does not create a deep trap, though, as evident from the shallowness of the transition energy level $\epsilon(V_1^{+/-})$ (Table 4).

CONCLUSIONS

Motivated by the importance of interfaces in layered perovskites, nanoparticles, and polycrystalline thin films, we characterized the formation of vacancies at the surface of a slab model and contrasted the results with the bulk of lead-halide perovskites using cubic and tetragonal CsPbI_3 as model structures. Our slab model is equivalent to the 2D Ruddlesden–Popper structure with six layers. Thus, we anticipate that the results will also be transferable to layered perovskites.

The free CsI-terminated surface does not act as a trap for free carriers since band edge states are not localized at the surface. The surface reconstruction creates an electric field that attracts electrons toward the surface but not strong enough to localize electrons at the surface. There is no significant perturbation of VBE states due to *p*-type vacancies (V_{Cs} , V_{pb} , and V_{pbI}) both at the surface and in the bulk. However, there is a notable attractive potential for electrons toward V_1 at the surface, especially in the case of the tetragonal phase. Formation energies of vacancies were evaluated with chemical potentials of species tailored to an aqueous solution. The chemical potentials were confined to a rather small region, which eliminated the largest source of uncertainty in previous calculations of defects' formation energies. The surface favors the formation of Cs vacancies, while Pb vacancies are more favorable in the bulk. The formation energy of iodine vacancies at the surface is very similar to that in the bulk. Lead–iodine divacancies (V_{pbI}^-) are expected to dominate over lead-only vacancies at the surfaces. The analysis of charged defects at the surface suggests pinning of the Fermi energy at the VBE and segregation of V_{Cs}^- and V_1^+ vacancies (both have a low formation energy of 0.25–0.4 eV). The predominant vacancies in the bulk are V_{pb}^{2-} and V_1^+ with a formation energy of about 0.5 eV. The chemical tolerance of our (defect) formation energy calculations is about 0.2 eV at most. Energy levels of dominant vacancies at the surface remain close to the band edges and do not form detrimental deep traps within the band gap. These states fall into the category of delocalized host states perturbed

by a screened Coulomb potential and follow band edges when the band gap is renormalized by SOC. There are no major differences between energy levels calculated with and without additional structural relaxation caused by changes in occupancy of electronic levels when transitioning from one charge state to another for dominant defects. The negligible structural relaxation between $q \pm 1$ states indicates a rather small Franck–Condon shift. Defects with a large Franck–Condon shift are likely to become centers of nonradiative recombination. These results explain the high optoelectronic performance of two-dimensional structures, nanoparticles, and polycrystalline thin films of lead-halide perovskites in spite of the abundance of interfaces in these materials.

Finally, it should be noted that there is no unique suggestion regarding the omission or inclusion of SOC when combined with DFT-PBE for the analysis of defects in this material system. The relativistic electronic structure of CBE in the slab is more resilient to the formation of surface states due to the mixing of Pb-p_{x,y,z} orbitals by the SOC Hamiltonian. Therefore, it is recommended to include SOC in the analysis of the spatial distribution of the wave function for CBE states and also for n-type defects. On the other hand, the formation energy of iodine vacancies is greatly underestimated (by ca. 1 eV) in a calculation at the DFT-PBE level of theory with SOC due to its large band gap error. It is, therefore, imperative not to combine PBE with SOC when computing the formation energy of n-type defects in this material system.

■ ASSOCIATED CONTENT

Data Availability Statement

VASP structure and output files are available from the Zenodo repository.⁷¹ The repository also includes the output of PyDEF 2 with an analysis of defect characteristics along with the PyDEF 2 main input file used in data processing. The modified version (fork) of PyDEF 2 code needed to reproduce this work is available from GitHub.⁵⁸ VASP structure files can be visualized using the Vesta program.⁹⁸

■ Supporting Information

The Supporting Information is available free of charge at <https://pubs.acs.org/doi/10.1021/acs.jpcc.3c06068>.

Spatial distribution of the VBE and CBE wave function probability densities $|\psi(\mathbf{r})|^2$ for the slab model calculated with and without defects at different levels of theory, the local structure of vacancies at the surface, details on calculation of the electrostatic charge correction for periodic slabs, the equivalent of Figure 3 for the tetragonal phase is presented with and without the electrostatic charge correction for periodic slabs and the following refs 62, 63, 65 and 69 were given credit in the Supporting Information (PDF)

■ AUTHOR INFORMATION

Corresponding Author

Oleg Rubel – Department of Materials Science and Engineering, McMaster University, Hamilton, Ontario L8S 4L8, Canada; orcid.org/0000-0001-5104-5602; Email: rubelo@mcmaster.ca

Author

Xavier Rocquefelte – Univ Rennes, CNRS, ISCR (Institut des Sciences Chimiques de Rennes) UMR 6226, Rennes 35700, France; orcid.org/0000-0003-0191-2354

Complete contact information is available at:
<https://pubs.acs.org/10.1021/acs.jpcc.3c06068>

Notes

The authors declare no competing financial interest.

■ ACKNOWLEDGMENTS

The authors are thankful to Camille Latouche and Théo Cavignac (University of Nantes) for a discussion about PyDEF 2. Calculations were performed using the Digital Research Alliance of Canada (Compute Canada) infrastructure supported by the Canada Foundation for Innovation under the John R. Evans Leaders Fund. X.R. acknowledges GENCI for granting access to the HPC resources of [TGCC/CINES/IDRIS] under the allocation 2022-A0130907682.

■ REFERENCES

- (1) Lany, S.; Zunger, A. Accurate prediction of defect properties in density functional supercell calculations. *Modelling Simul. Mater. Sci. Eng.* **2009**, *17*, 084002.
- (2) Freysoldt, C.; Grabowski, B.; Hickel, T.; Neugebauer, J.; Kresse, G.; Janotti, A.; Van de Walle, C. G. First-principles calculations for point defects in solids. *Rev. Mod. Phys.* **2014**, *86*, 253–305.
- (3) Yang, J.; Youssef, M.; Yildiz, B. Predicting point defect equilibria across oxide hetero-interfaces: model system of ZrO₂/Cr₂O₃. *Phys. Chem. Chem. Phys.* **2017**, *19*, 3869–3883.
- (4) Gao, Y.; Sun, D.; Jiang, X.; Zhao, J. Ab initio analytic calculation of point defects in AlGaN/GaN heterointerfaces. *J. Phys.: Condens. Matter* **2021**, *33*, 035002.
- (5) Komsa, H.-P.; Pasquarello, A. Finite-size supercell correction for charged defects at surfaces and interfaces. *Phys. Rev. Lett.* **2013**, *110*, 095505.
- (6) Freysoldt, C.; Mishra, A.; Ashton, M.; Neugebauer, J. Generalized dipole correction for charged surfaces in the repeated-slab approach. *Phys. Rev. B* **2020**, *102*, 045403.
- (7) Cho, Y.; Jung, H. R.; Jo, W. Halide perovskite single crystals: growth, characterization, and stability for optoelectronic applications. *Nanoscale* **2022**, *14*, 9248–9277.
- (8) Yin, W.-J.; Shi, T.; Yan, Y. Unique properties of halide perovskites as possible origins of the superior solar cell performance. *Adv. Mater.* **2014**, *26*, 4653–4658.
- (9) Agiorgousis, M. L.; Sun, Y.-Y.; Zeng, H.; Zhang, S. Strong covalency-induced recombination centers in perovskite solar cell material CH₃NH₃PbI₃. *J. Am. Chem. Soc.* **2014**, *136*, 14570–14575.
- (10) Yin, W.-J.; Shi, T.; Yan, Y. Unusual defect physics in CH₃NH₃PbI₃ perovskite solar cell absorber. *Appl. Phys. Lett.* **2014**, *104*, 063903.
- (11) Du, M.-H. Density functional calculations of native defects in CH₃NH₃PbI₃: effects of spin–orbit coupling and self-interaction error. *J. Phys. Chem. Lett.* **2015**, *6*, 1461–1466.
- (12) Brandt, R. E.; Stevanović, V.; Ginley, D. S.; Buonassisi, T. Identifying defect-tolerant semiconductors with high minority-carrier lifetimes: beyond hybrid lead halide perovskites. *MRS Commun.* **2015**, *5*, 265–275.
- (13) Kang, J.; Wang, L.-W. High defect tolerance in lead halide perovskite CsPbBr₃. *J. Phys. Chem. Lett.* **2017**, *8*, 489–493.
- (14) Walsh, A.; Zunger, A. Instilling defect tolerance in new compounds. *Nat. Mater.* **2017**, *16*, 964–967.
- (15) Li, Y.; Zhang, C.; Zhang, X.; Huang, D.; Shen, Q.; Cheng, Y.; Huang, W. Intrinsic point defects in inorganic perovskite CsPbI₃ from first-principles prediction. *Appl. Phys. Lett.* **2017**, *111*, 162106.
- (16) Meggiolaro, D.; Motti, S. G.; Mosconi, E.; Barker, A. J.; Ball, J.; Andrea Riccardo Perini, C.; Deschler, F.; Petrozza, A.; De Angelis, F. Iodine chemistry determines the defect tolerance of lead-halide perovskites. *Energy Environ. Sci.* **2018**, *11*, 702–713.
- (17) Zhang, X.; Munir, R.; Xu, Z.; Liu, Y.; Tsai, H.; Nie, W.; Li, J.; Niu, T.; Smilgies, D.-M.; Kanatzidis, M. G.; et al. Phase transition

- control for high performance Ruddlesden-Popper perovskite solar cells. *Adv. Mater.* **2018**, *30*, 1707166.
- (18) Aygüler, M. F.; Weber, M. D.; Puscher, B. M. D.; Medina, D. D.; Docampo, P.; Costa, R. D. Light-emitting electrochemical cells based on hybrid lead halide perovskite nanoparticles. *J. Phys. Chem. C* **2015**, *119*, 12047–12054.
- (19) Protesescu, L.; Yakunin, S.; Bodnarchuk, M. I.; Krieg, F.; Caputo, R.; Hendon, C. H.; Yang, R. X.; Walsh, A.; Kovalenko, M. V. Nanocrystals of cesium lead halide perovskites (CsPbX_3 , X = Cl, Br, and I): novel optoelectronic materials showing bright emission with wide color gamut. *Nano Lett.* **2015**, *15*, 3692–3696.
- (20) De Wolf, S.; Holovsky, J.; Moon, S.-J.; Löper, P.; Niesen, B.; Ledinsky, M.; Haug, F.-J.; Yum, J.-H.; Ballif, C. Organometallic halide perovskites: sharp optical absorption edge and its relation to photovoltaic performance. *J. Phys. Chem. Lett.* **2014**, *5*, 1035–1039.
- (21) Zhao, L.; Tang, P.; Luo, D.; Dar, M. I.; Eickemeyer, F. T.; Arora, N.; Hu, Q.; Luo, J.; Liu, Y.; Zakeeruddin, S. M.; et al. Enabling full-scale grain boundary mitigation in polycrystalline perovskite solids. *Sci. Adv.* **2022**, *8*, No. eab03733.
- (22) Lu, H.; Krishna, A.; Zakeeruddin, S. M.; Grätzel, M.; Hagfeldt, A. Compositional and interface engineering of organic-inorganic lead halide perovskite solar cells. *iScience* **2020**, *23*, 101359.
- (23) Park, K.; Lee, J.-H.; Lee, J.-W. Surface defect engineering of metal halide perovskites for photovoltaic applications. *ACS Energy Lett.* **2022**, *7*, 1230–1239.
- (24) Jiang, Q.; Tong, J.; Xian, Y.; Kerner, R. A.; Dunfield, S. P.; Xiao, C.; Scheidt, R. A.; Kuciauskas, D.; Wang, X.; Hautzinger, M. P.; et al. Surface reaction for efficient and stable inverted perovskite solar cells. *Nature* **2022**, *611*, 278–283.
- (25) Chen, R.; Wang, J.; Liu, Z.; Ren, F.; Liu, S.; Zhou, J.; Wang, H.; Meng, X.; Zhang, Z.; Guan, X.; et al. Reduction of bulk and surface defects in inverted methylammonium- and bromide-free formamidinium perovskite solar cells. *Nat. Energy* **2023**, *8*, 839–849.
- (26) Buin, A.; Pietsch, P.; Xu, J.; Voznyy, O.; Ip, A. H.; Comin, R.; Sargent, E. H. Materials processing routes to trap-free halide perovskites. *Nano Lett.* **2014**, *14*, 6281–6286.
- (27) Haruyama, J.; Sodeyama, K.; Han, L.; Tateyama, Y. Termination dependence of tetragonal $\text{CH}_3\text{NH}_3\text{PbI}_3$ surfaces for perovskite solar cells. *J. Phys. Chem. Lett.* **2014**, *5*, 2903–2909.
- (28) Meggiolaro, D.; Mosconi, E.; Proppe, A. H.; Quintero-Bermudez, R.; Kelley, S. O.; Sargent, E. H.; De Angelis, F. Energy level tuning at the MAPbI_3 perovskite/contact interface using chemical treatment. *ACS Energy Lett.* **2019**, *4*, 2181–2184.
- (29) Stoumpos, C. C.; Soe, C. M. M.; Tsai, H.; Nie, W.; Blancon, J.-C.; Cao, D. H.; Liu, F.; Traoré, B.; Katan, C.; Even, J.; et al. High members of the 2D Ruddlesden-Popper halide perovskites: synthesis, optical properties, and solar cells of $(\text{CH}_3(\text{CH}_2)_3\text{NH}_3)_2(\text{CH}_3\text{NH}_3)_4\text{Pb}_5\text{I}_{16}$. *Chem.* **2017**, *2*, 427–440.
- (30) Mosconi, E.; Meggiolaro, D.; Snaith, H. J.; Stranks, S. D.; De Angelis, F. Light-induced annihilation of Frenkel defects in organolead halide perovskites. *Energy Environ. Sci.* **2016**, *9*, 3180–3187.
- (31) Perez, C. M.; Ghosh, D.; Prezhdo, O.; Nie, W.; Tretiak, S.; Neukirch, A. Point defects in two-dimensional Ruddlesden-Popper perovskites explored with ab initio calculations. *J. Phys. Chem. Lett.* **2022**, *13*, 5213–5219.
- (32) ten Brinck, S.; Zaccaria, F.; Infante, I. Defects in lead halide perovskite nanocrystals: analogies and (many) differences with the bulk. *ACS Energy Lett.* **2019**, *4*, 2739–2747.
- (33) Song, J.; Qian, J.; Liu, L.; Huang, D.; Li, Z.; Xu, B.; Tian, W. Theoretical study on defect properties of two-dimensional multilayer Ruddlesden-Popper lead iodine perovskite. *Comput. Mater. Sci.* **2021**, *194*, 110457.
- (34) Trots, D. M.; Myagkota, S. V. High-temperature structural evolution of caesium and rubidium triiodoplumbates. *J. Phys. Chem. Solids* **2008**, *69*, 2520–2526.
- (35) Franck, J.; Dymond, E. G. Elementary processes of photochemical reactions. *Trans. Faraday Soc.* **1926**, *21*, 536.
- (36) Condon, E. A theory of intensity distribution in band systems. *Phys. Rev.* **1926**, *28*, 1182–1201.
- (37) Hohenberg, P.; Kohn, W. Inhomogeneous electron gas. *Phys. Rev.* **1964**, *136*, B864–B871.
- (38) Kohn, W.; Sham, L. J. Self-consistent equations including exchange and correlation effects. *Phys. Rev.* **1965**, *140*, A1133–A1138.
- (39) Perdew, J. P.; Burke, K.; Ernzerhof, M. Generalized gradient approximation made simple. *Phys. Rev. Lett.* **1996**, *77*, 3865–3868.
- (40) Kresse, G.; Hafner, J. Ab initio molecular dynamics for liquid metals. *Phys. Rev. B* **1993**, *47*, 558–561.
- (41) Kresse, G.; Furthmüller, J. Efficiency of ab-initio total energy calculations for metals and semiconductors using a plane-wave basis set. *Comput. Mater. Sci.* **1996**, *6*, 15–50.
- (42) Kresse, G.; Furthmüller, J. Efficient iterative schemes for ab initio total-energy calculations using a plane-wave basis set. *Phys. Rev. B* **1996**, *54*, 11169–11186.
- (43) Grimme, S.; Antony, J.; Ehrlich, S.; Krieg, H. A consistent and accurate ab initio parametrization of density functional dispersion correction (DFT-D) for the 94 elements H–Pu. *J. Chem. Phys.* **2010**, *132*, 154104.
- (44) Grimme, S.; Ehrlich, S.; Goerigk, L. Effect of the damping function in dispersion corrected density functional theory. *J. Comput. Chem.* **2011**, *32*, 1456–1465.
- (45) Kresse, G.; Joubert, D. From ultrasoft pseudopotentials to the projector augmented-wave method. *Phys. Rev. B* **1999**, *59*, 1758–1775.
- (46) Monkhorst, H. J.; Pack, J. D. Special points for Brillouin-zone integrations. *Phys. Rev. B* **1976**, *13*, 5188–5192.
- (47) Yang, R. X.; Skelton, J. M.; da Silva, E. L.; Frost, J. M.; Walsh, A. Assessment of dynamic structural instabilities across 24 cubic inorganic halide perovskites. *J. Chem. Phys.* **2020**, *152*, 024703.
- (48) Ming, C.; Wang, H.; West, D.; Zhang, S.; Sun, Y.-Y. Defect tolerance in CsPbI_3 : reconstruction of the potential energy landscape and band degeneracy in spin-orbit coupling. *J. Mater. Chem. A* **2022**, *10*, 3018–3024.
- (49) Sutton, R. J.; Filip, M. R.; Haghhighirad, A. A.; Sakai, N.; Wenger, B.; Giustino, F.; Snaith, H. J. Cubic or orthorhombic? Revealing the crystal structure of metastable black-phase CsPbI_3 by theory and experiment. *ACS Energy Lett.* **2018**, *3*, 1787–1794.
- (50) Stoumpos, C. C.; Malliakas, C. D.; Kanatzidis, M. G. Semiconducting Tin and Lead Iodide Perovskites with Organic Cations: Phase Transitions, High Mobilities, and Near-Infrared Photoluminescent Properties. *Inorg. Chem.* **2013**, *S2*, 9019–9038.
- (51) Whitfield, P. S.; Herron, N.; Guise, W. E.; Page, K.; Cheng, Y. Q.; Milas, I.; Crawford, M. K. Structures, phase transitions and tricritical behavior of the hybrid perovskite methyl ammonium lead iodide. *Sci. Rep.* **2016**, *6*, 35685.
- (52) Zheng, C.; Yu, S.; Rubel, O. Structural dynamics in hybrid halide perovskites: bulk Rashba splitting, spin texture, and carrier localization. *Phys. Rev. Materials* **2018**, *2*, 114604.
- (53) Jain, A.; Ong, S. P.; Hautier, G.; Chen, W.; Richards, W. D.; Dacek, S.; Cholia, S.; Gunter, D.; Skinner, D.; Ceder, G.; et al. Commentary: The Materials Project: A materials genome approach to accelerating materials innovation. *APL Mater.* **2013**, *1*, 011002.
- (54) Heyd, J.; Scuseria, G. E.; Ernzerhof, M. Hybrid functionals based on a screened Coulomb potential. *J. Chem. Phys.* **2003**, *118*, 8207–8215.
- (55) Kruckau, A. V.; Vydrov, O. A.; Izmaylov, A. F.; Scuseria, G. E. Influence of the exchange screening parameter on the performance of screened hybrid functionals. *J. Chem. Phys.* **2006**, *125*, 224106.
- (56) Péan, E.; Vidal, J.; Jobic, S.; Latouche, C. Presentation of the PyDEF post-treatment Python software to compute publishable charts for defect energy formation. *Chem. Phys. Lett.* **2017**, *671*, 124–130.
- (57) Stolaroff, A.; Jobic, S.; Latouche, C. PyDEF 2.0: an easy to use post-treatment software for publishable charts featuring a graphical user interface. *J. Comput. Chem.* **2018**, *39*, 2251–2261.
- (58) Rubel, O. A Modified Version (fork) of PyDEF 2 for VASP, 2023. <https://github.com/rubel75/PyDEF-2.0> (accessed Dec 20, 2023).

- (59) Zhang, S.; Northrup, J. Chemical potential dependence of defect formation energies in GaAs: application to Ga self-diffusion. *Phys. Rev. Lett.* **1991**, *67*, 2339–2342.
- (60) Lany, S.; Zunger, A. Assessment of correction methods for the band-gap problem and for finite-size effects in supercell defect calculations: case studies for ZnO and GaAs. *Phys. Rev. B* **2008**, *78*, 235104.
- (61) Persson, C.; Zhao, Y.-J.; Lany, S.; Zunger, A. n-type doping of CuInSe₂ and CuGaSe₂. *Phys. Rev. B* **2005**, *72*, 035211.
- (62) Makov, G.; Payne, M. C. Periodic boundary conditions in ab initio calculations. *Phys. Rev. B* **1995**, *51*, 4014–4022.
- (63) Srikanth, M.; Ozório, M. S.; Da Silva, J. L. F. Optical and dielectric properties of lead perovskite and iodoplumbate complexes: an ab initio study. *Phys. Chem. Chem. Phys.* **2020**, *22*, 18423–18434.
- (64) Noh, J.-Y.; Kim, H.; Kim, Y.-S. Stability and electronic structures of native defects in single-layer MoS₂. *Phys. Rev. B* **2014**, *89*, 205417.
- (65) Freysoldt, C.; Neugebauer, J. First-principles calculations for charged defects at surfaces, interfaces, and two-dimensional materials in the presence of electric fields. *Phys. Rev. B* **2018**, *97*, 205425.
- (66) Chagas da Silva, M.; Lorke, M.; Aradi, B.; Farzalipour Tabriz, M.; Frauenheim, T.; Rubio, A.; Rocca, D.; Deák, P. Self-consistent potential correction for charged periodic systems. *Phys. Rev. Lett.* **2021**, *126*, 076401.
- (67) Freysoldt, C.; Neugebauer, J.; Tan, A. M. Z.; Hennig, R. G. Limitations of empirical supercell extrapolation for calculations of point defects in bulk, at surfaces, and in two-dimensional materials. *Phys. Rev. B* **2022**, *105*, 014103.
- (68) Komsa, H.-P.; Rantala, T. T.; Pasquarello, A. Finite-size supercell correction schemes for charged defect calculations. *Phys. Rev. B* **2012**, *86*, 045112.
- (69) Freysoldt, C.; Neugebauer, J.; Van de Walle, C. G. Fully ab initio finite-size corrections for charged-defect supercell calculations. *Phys. Rev. Lett.* **2009**, *102*, 016402.
- (70) Ciftja, O. A result for the Coulomb electrostatic energy of a uniformly charged disk. *Results Phys.* **2017**, *7*, 1674–1675.
- (71) Rubel, O.; Rocquefelte, X. Defect tolerance of lead-halide perovskite (100) surface relative to bulk: band bending, surface states, and characteristics of vacancies (dataset), 2023, <https://doi.org/10.5281/zenodo.8329348> (accessed Dec 20, 2023).
- (72) Rubel, O. VASPtools. <https://github.com/rubel75/VASPtools> (accessed Dec 20, 2023).
- (73) Ruddlesden, S. N.; Popper, P. The compound Sr₃Ti₂O₇ and its structure. *Acta Crystallogr.* **1958**, *11*, 54–55.
- (74) Frost, J. M.; Butler, K. T.; Brivio, F.; Hendon, C. H.; van Schilfgaarde, M.; Walsh, A. Atomistic origins of high-performance in hybrid halide perovskite solar cells. *Nano Lett.* **2014**, *14*, 2584–2590.
- (75) Liu, S.; Zheng, F.; Koocher, N. Z.; Takenaka, H.; Wang, F.; Rappe, A. M. Ferroelectric domain wall induced band gap reduction and charge separation in organometal halide perovskites. *J. Phys. Chem. Lett.* **2015**, *6*, 693–699.
- (76) Yang, Z.; Surrenti, A.; Galkowski, K.; Miyata, A.; Portugall, O.; Sutton, R. J.; Haghghirad, A. A.; Snaith, H. J.; Maude, D. K.; Plochocka, P.; et al. Impact of the halide cage on the electronic properties of fully inorganic cesium lead halide perovskites. *ACS Energy Lett.* **2017**, *2*, 1621–1627.
- (77) Even, J.; Pedesseau, L.; Jancu, J.-M.; Katan, C. Importance of spin-orbit coupling in hybrid organic/inorganic perovskites for photovoltaic applications. *J. Phys. Chem. Lett.* **2013**, *4*, 2999–3005.
- (78) Dymshits, A.; Rotem, A.; Etgar, L. High voltage in hole conductor free organo metal halide perovskite solar cells. *J. Mater. Chem. A* **2014**, *2*, 20776–20781.
- (79) Kim, D.; Yun, J.-H.; Lyu, M.; Kim, J.; Lim, S.; Yun, J. S.; Wang, L.; Seidel, J. Probing facet-dependent surface defects in MAPbI₃ perovskite single crystals. *J. Phys. Chem. C* **2019**, *123*, 14144–14151.
- (80) Jackson, A. J.; Walsh, A. Oxidation of GaN: an ab initio thermodynamic approach. *Phys. Rev. B* **2013**, *88*, 165201.
- (81) Pourbaix, M. *Atlas of Electrochemical Equilibria in Aqueous Solutions*, 2nd ed.; National Association of Corrosion Engineers, 1974.
- (82) Cordfunke, E. H. P.; Prins, G. The thermochemical properties of caesium iodide. I. Thermodynamic functions of solid CsI. *Thermochim. Acta* **1985**, *90*, 169–176.
- (83) Chase, M. W. *NIST-JANAF Thermochemical Tables J. Phys. Chem. Ref. Data*, 4th ed.; American Institute of Physics, Monograph 9, 1998; pp 1–1951.
- (84) Wang, B.; Novendra, N.; Navrotsky, A. Energetics, structures, and phase transitions of cubic and orthorhombic cesium lead iodide (CsPbI₃) polymorphs. *J. Am. Chem. Soc.* **2019**, *141*, 14501–14504.
- (85) CRC Handbook of Chemistry and Physics, 97th ed.; Haynes, W. M., Lide, D. R., Bruno, T. J., Eds.; CRC Press, 2016–2017.
- (86) Wu, X.; Ming, C.; Shi, J.; Wang, H.; West, D.; Zhang, S.; Sun, Y.-Y. Defects in statically unstable solids: the case for cubic perovskite α -CsPbI₃. *Chin. Phys. Lett.* **2022**, *39*, 046101.
- (87) Hellström, M.; Spångberg, D.; Hermansson, K.; Broqvist, P. Band-filling correction method for accurate adsorption energy calculations: a Cu/ZnO case study. *J. Chem. Theory Comput.* **2013**, *9*, 4673–4678.
- (88) Perdew, J. P.; Parr, R. G.; Levy, M.; Balduz, J. L. Density-functional theory for fractional particle number: derivative discontinuities of the energy. *Phys. Rev. Lett.* **1982**, *49*, 1691–1694.
- (89) Schulte, F. K. Chemical potentials and workfunctions of metal surfaces in the theory of an inhomogeneous electron gas. *J. Phys. C: Solid State Phys.* **1974**, *7*, L370–L373.
- (90) Janak, J. F. Proof that $\partial E/\partial n_i = \epsilon$ in density-functional theory. *Phys. Rev. B* **1978**, *18*, 7165–7168.
- (91) Gerstmann, U.; Deák, P.; Rurali, R.; Aradi, B.; Frauenheim, T.; Overhof, H. Charge corrections for supercell calculations of defects in semiconductors. *Phys. B* **2003**, *340*–342, 190–194.
- (92) Lyons, J. L.; Janotti, A.; Van de Walle, C. G. Carbon impurities and the yellow luminescence in GaN. *Appl. Phys. Lett.* **2010**, *97*, 152108.
- (93) Alkauskas, A.; McCluskey, M. D.; Van de Walle, C. G. Tutorial: Defects in semiconductors—combining experiment and theory. *J. Appl. Phys.* **2016**, *119*, 181101.
- (94) Xie, Z.; Feng, K.; Xiong, Y.; Chen, X.; Liang, Y.; Abid, K.; Xu, L. A high Seebeck voltage thermoelectric module with p-type and n-type MAPbI₃ perovskite single crystals. *Adv. Electron. Mater.* **2021**, *7*, 2001003.
- (95) Peña-Camargo, F.; Thiesbrummel, J.; Hempel, H.; Musienko, A.; Le Corre, V. M.; Diekmann, J.; Warby, J.; Unold, T.; Lang, F.; Neher, D.; et al. Revealing the doping density in perovskite solar cells and its impact on device performance. *Appl. Phys. Rev.* **2022**, *9*, 021409.
- (96) Murphy, N. C.; Wortis, R.; Atkinson, W. A. Generalized inverse participation ratio as a possible measure of localization for interacting systems. *Phys. Rev. B* **2011**, *83*, 184206.
- (97) Pashartis, C.; Rubel, O. Localization of electronic states in III-V semiconductor alloys: a comparative study. *Phys. Rev. Appl.* **2017**, *7*, 064011.
- (98) Momma, K.; Izumi, F. VESTA3 for three-dimensional visualization of crystal, volumetric and morphology data. *J. Appl. Crystallogr.* **2011**, *44*, 1272–1276.

Supplementary information for publication

Title: **Defect Tolerance of Lead-Halide Perovskite (100) Surface Relative to Bulk: Band Bending, Surface States, and Characteristics of Vacancies**

Authors: *Oleg Rubel[†]* and *Xavier Rocquefelte[‡]*

Affiliations: [†]Department of Materials Science and Engineering, McMaster University, 1280 Main Street West, Hamilton, Ontario L8S 4L8, Canada; [‡]Univ Rennes, CNRS, ISCR (Institut des Sciences Chimiques de Rennes) UMR 6226, 263 Av. Général Leclerc, 35700 Rennes, France.

Figures S1–S3, S6, and S7 show the atom-resolved DFT wave functions $|\psi_{n,\mathbf{k},\alpha}(z)|^2$ for the VBE and CBE, normalized such that $\int \sum_{\alpha} |\psi_{n,\mathbf{k},\alpha}(z)|^2 dz = 1$. Here, n is the band index, \mathbf{k} is the electron wave vector, and α is the atom label that runs over all atoms. The local structure of vacancies at the surface is shown in Fig. S5. Additional tests were performed to confirm that the results in Fig. S6 remain valid when a dipole correction is activated (VASP tags LDIPOL=.TRUE., IDIPOL=3, DIPOL=0.5 0.5 0.5).

Figure S4 shows the correlation between the formation energy of a neutral iodine vacancy at a slab surface and the calculated band gap. Therefore, it is important to select an appropriate structural model in combination with the appropriate level of theory to obtain reliable results.

The periodic electrostatic energy for charged slab models U_{per} was calculated using the `sxdefectalign2d` package^{65,69} version 1.1. The model excess charge density $\delta\rho(z)$ was approximated by a superposition of Gaussian functions. (Note that `sxdefectalign2d` uses a charge convention with a negative sign for positive charge.) The dielectric profile was approximated by a rectangular shape (Fig. S8), assuming an isotropic relative dielectric constant of 6.3⁶³ for the slab materials. A cut-off energy of 40 Ry was selected to match the discretization of the Fourier space along the z -axis to that in VASP `LOCPO`T files. A large in-plane Gaussian broadening of $\beta_{\parallel} = 200$ bohr in the lateral direction was selected to repre-

sent charge delocalization. The model potential $\delta\phi(z)$ was calculated by `sxdefectalign2d` via solving a periodic Poisson's equation.

The listing below shows a sample of `sxdefectalign2d` input file `system.sx` for a charged iodine vacancy (without SOC). The total charge $\sum Q = -1$ implies the positively charged defect (deficiency of $1e$). The excess charge is approximated by 11 Gaussian functions, each with a spread of 3 bohr along the z axis:

```
slab {
    fromZ = 17.827539465159465;
    toZ = 78.59547174181203;
    epsilon = 6.3;
}

isolated {
    fromZ = 48.21150560348575;
    toZ = 87.47975407924827;
}

charge {
    posZ = 20.856600667379407;
    Q = -0.09090909090909091;
    betaZ = 3;
    betaPara = 200;
}

charge {
    posZ = 21.082790309866194;
    Q = -0.09090909090909091;
    betaZ = 3;
    betaPara = 200;
}
```

```

charge {
    posZ = 21.65211298378684;
    Q = -0.09090909090909091;
    betaZ = 3;
    betaPara = 200;
}

charge {
    posZ = 57.7869527991119;
    Q = -0.09090909090909091;
    betaZ = 3;
    betaPara = 200;
}

charge {
    posZ = 75.44635482632142;
    Q = -0.09090909090909091;
    betaZ = 3;
    betaPara = 200;
}

charge {
    posZ = 74.2780842525695;
    Q = -0.09090909090909091;
    betaZ = 3;
    betaPara = 200;
}

charge {
    posZ = 74.86934094464065;
    Q = -0.09090909090909091;
}

```

```

betaZ = 3;
betaPara = 200;
}

charge {
    posZ = 75.44864738923125;
    Q = -0.09090909090909091;
    betaZ = 3;
    betaPara = 200;
}

charge {
    posZ = 75.41614185661757;
    Q = -0.09090909090909091;
    betaZ = 3;
    betaPara = 200;
}

charge {
    posZ = 75.2970505657695;
    Q = -0.09090909090909091;
    betaZ = 3;
    betaPara = 200;
}

charge {
    posZ = 75.50571889448972;
    Q = -0.09090909090909091;
    betaZ = 3;
    betaPara = 200;
}

```

The code is executed using the command

```
sxdefectalign2d --vref LOCPOT --vdef LOCPOTchrg_m1 --vasp --ecut 40
```

The sample output is listed below:

```
VASP mesh: 140 x 140 x 384
cell defect = [a1={33.0657,0,0},a2={0,33.0657,0},a3={0,0,96.364}]
VASP mesh: 140 x 140 x 384
cell bulk = [a1={33.0657,0,0},a2={0,33.0657,0},a3={0,0,96.364}]
Periodic supercell taken from LOCPOTchrg_p1
[a1={33.0657,0,0},a2={0,33.0657,0},a3={0,0,96.364}]
Cutoff = 40 Ry
N = 396
--- Periodic
Q=-1
short-range potential with averaging width = 2 bohr
Slope bottom (@z=48.182)= 0.00456743 eV/bohr, value = -0.00937142 eV
Slope top (@z=87.6037) = 0.00198296 eV/bohr, value = -0.070616 eV
---
--- Isolated
Isolated from 48.1820175594 to 87.6036682897 (162 points)
Q=-0.727204072125
Interface: 78.5954717418
zL = 48.1820175594 eps = 6.3
E-field dependence left: zeff = 73.9587635068
zR = 87.6036682897 eps = 1
E-field dependence right: zeff = 77.8594863077
---
isolated energy = 0.00853691299722 eV
```

```
periodic energy = 0.108846350821 eV
```

```
iso - periodic energy = -0.100309437824 eV
```

We are interested in the periodic energy $U_{\text{per}} = 0.11$ eV. This energy needs to be *subtracted* from the formation energy of a charged defect. By including this correction, we obtain the transition energy level $\varepsilon(V_I^{+/0}) = E_{\text{CBE}} - 0.08$ eV instead of $E_{\text{CBE}} - 0.19$ eV reported in Table 4 for the tetragonal slab model without SOC. The isolated energy is not exactly zero due to the finite size of β_{\parallel} , but it becomes zero in the limit of $\beta_{\parallel} \rightarrow \infty$. The output file `vline-eV.dat` contains the model potential $\delta\phi$, the DFT potential ΔV_{DFT} , and their difference. We used an auxiliary Python code to optimize positions of the Gaussian functions and minimize the residual between $\delta\phi$ and ΔV_{DFT} . Results for other charged defects in the $2\sqrt{2} \times 2\sqrt{2} \times 5$ tetragonal slab are presented in Figs. S9 and S10 (without and with SOC, respectively).

If the periodic slab correction (Fig. S9) was applied to energies of charged defects, all energies of defects with the charge ± 1 would be shifted down by ca. 0.05–0.1 eV as shown in Fig. S11 for the tetragonal phase. The correction magnitude increases to 0.33–0.36 eV for the formation energy of V_{Pb}^{2-} (Figs. S9 and S10), which follows the q^2 scaling.⁶²

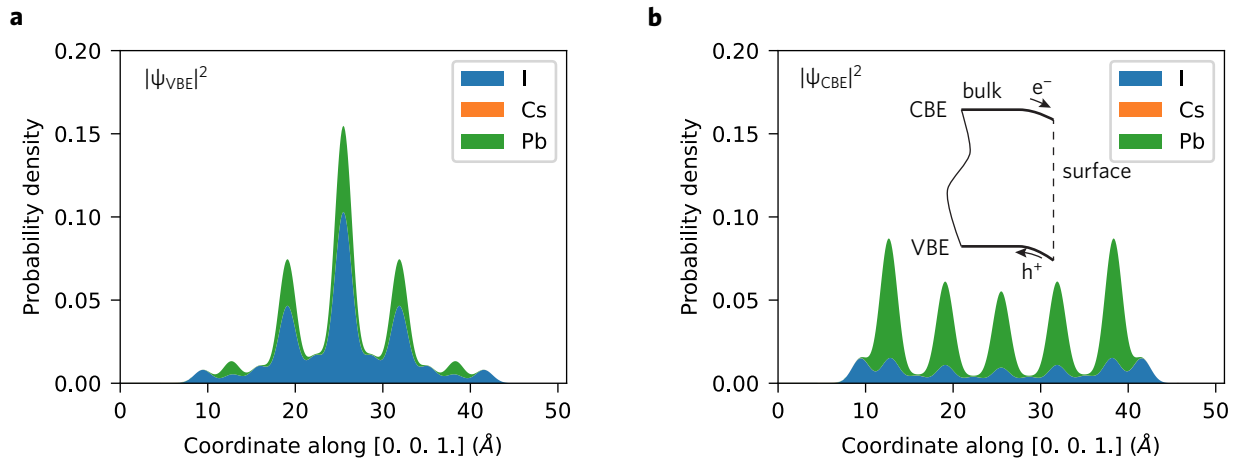


Figure S1: Wave function distribution in a slab of tetragonal CsPbI₃ calculated with PBE-SOC: (a,b) band edges (VBE and CBE) with surface reconstruction calculated at HSE06 level of theory, (c,d) band edges without surface reconstruction calculated at PBE level of theory.

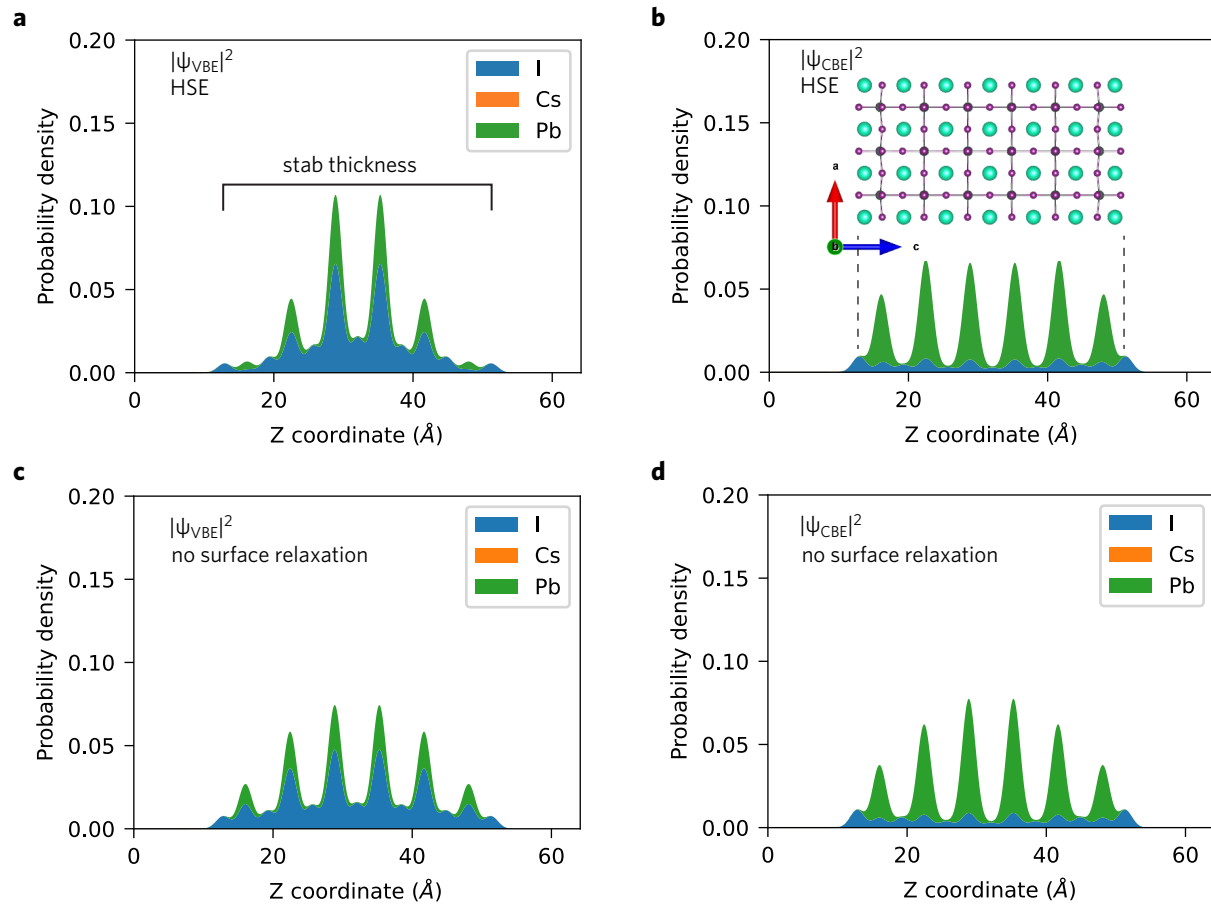


Figure S2: Wave function distribution in a slab of cubic CsPbI_3 calculated with SOC: (a,b) band edges (VBE and CBE) with surface reconstruction calculated at HSE06 level of theory, (c,d) band edges without surface reconstruction calculated at PBE level of theory.

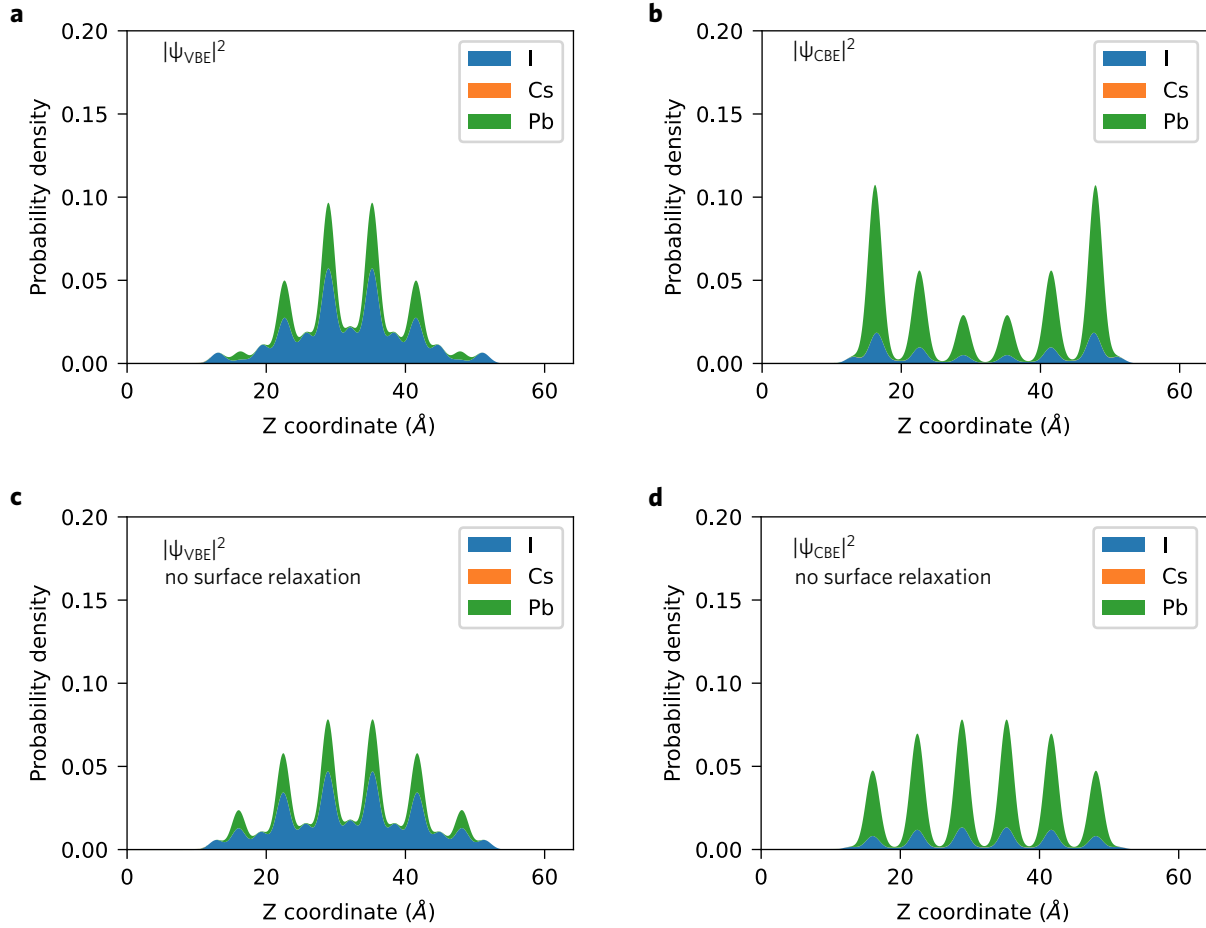


Figure S3: Wave function distribution in a slab of cubic CsPbI_3 calculated **without** SOC at PBE level of theory: (a,b) band edges (VBE and CBE) with surface reconstruction, (c,d) band edges without surface reconstruction.

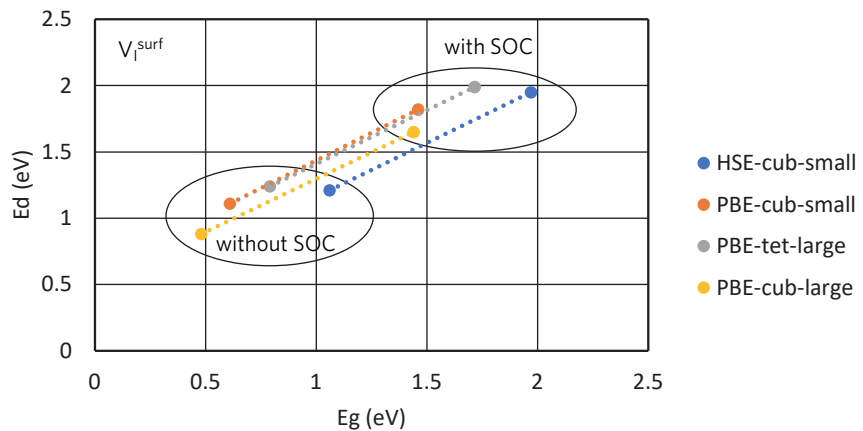


Figure S4: Formation energy of the neutral iodine vacancy at the slab surface correlated with the calculated band gap. The ‘small’ , ‘large’ cubic and ‘large’ tetragonal slab models refer to the sizes $2 \times 2 \times 3$, $3 \times 3 \times 6$, and $2\sqrt{2} \times 2\sqrt{2} \times 5$, respectively.

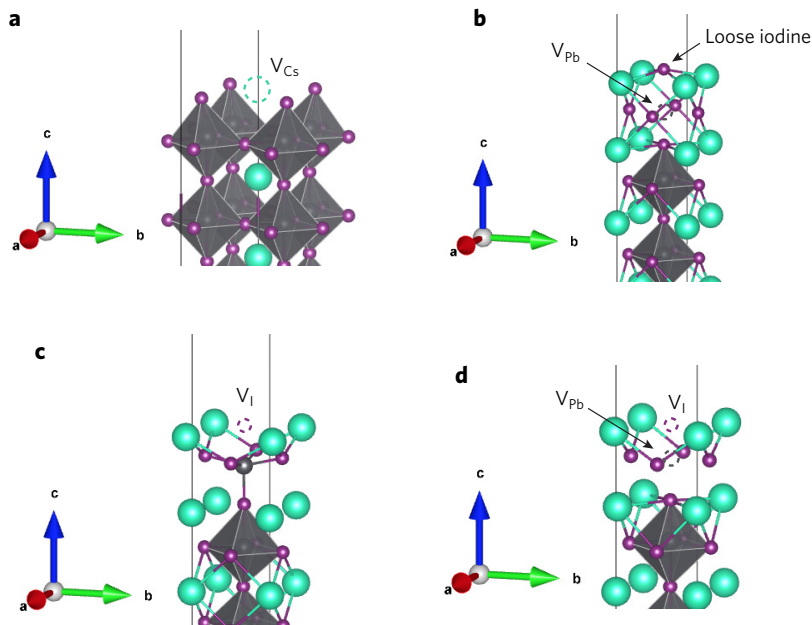


Figure S5: Local structure of surface defects: (a) cesium vacancy, (b) lead vacancy, (c) iodine vacancy, (d) lead-iodine divacancy. Only a small fragment in the immediate vicinity of defects is shown.

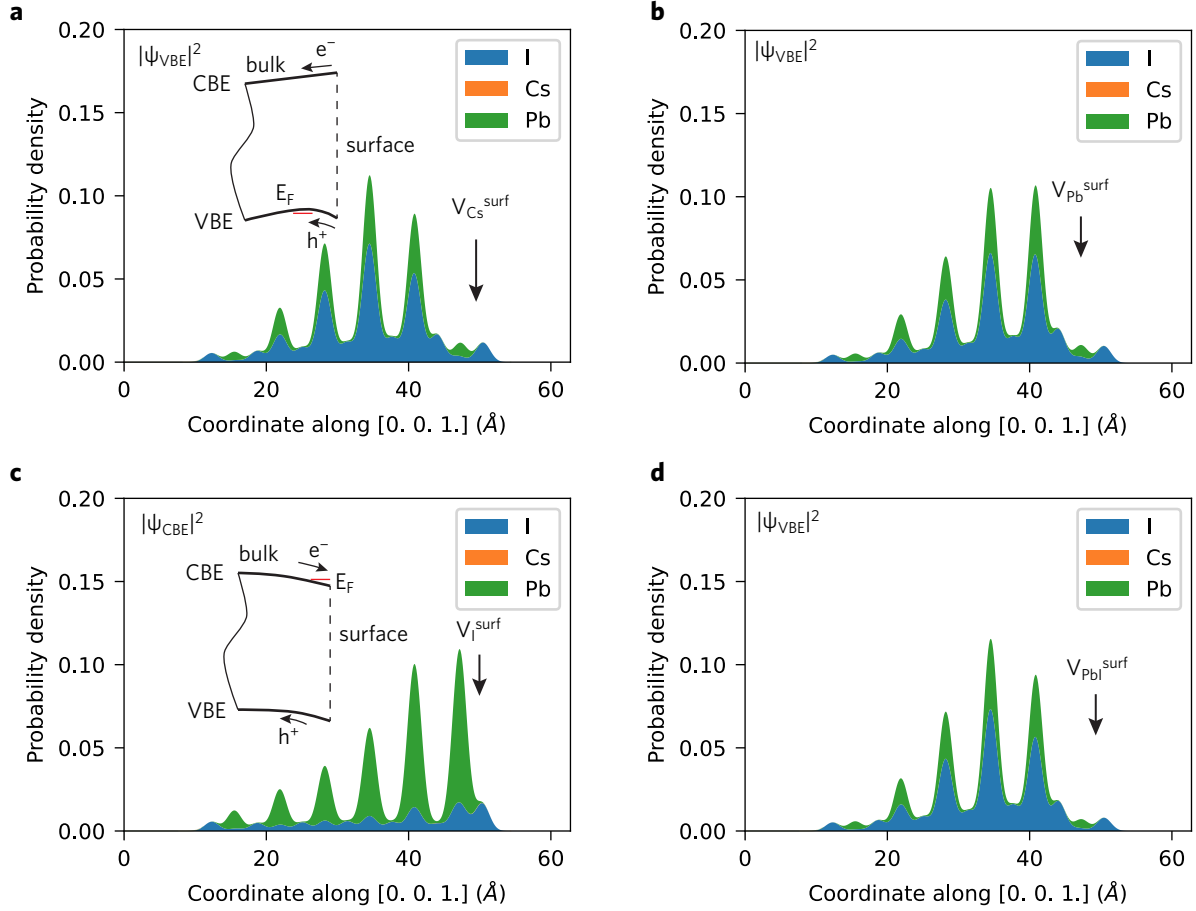


Figure S6: Wave function distribution at band edges (VBE and CBE) in a slab of cubic CsPbI_3 with surface defects: (a) V_{Cs} , (b) V_{Pb} , (c) V_{I} , and (d) V_{PbI} . The location of defects is marked with arrows. The calculations include SOC. Inset shows a schematic band diagram.

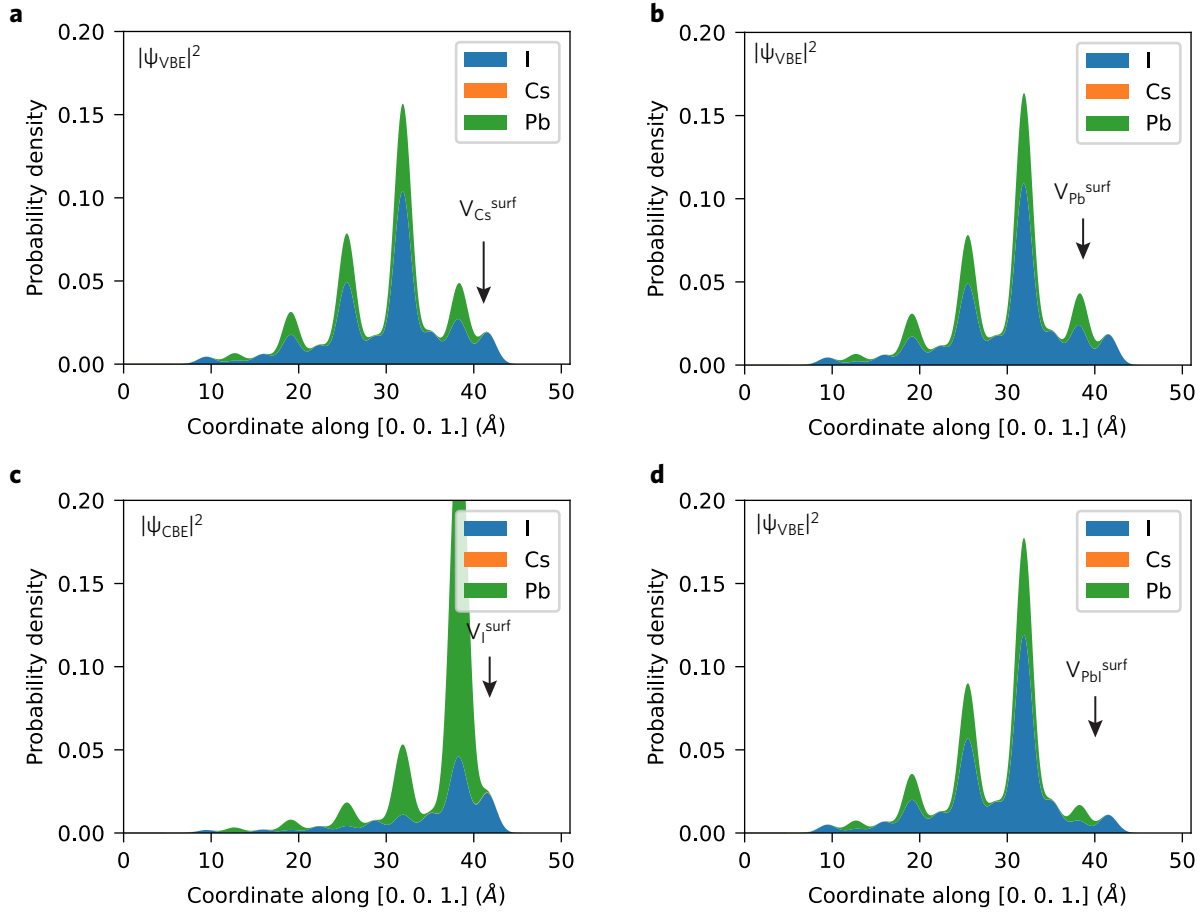


Figure S7: Wave function distribution at band edges (VBE and CBE) in a slab of tetragonal CsPbI_3 with surface defects: (a) V_{Cs} , (b) V_{Pb} , (c) V_{I} , and (d) V_{PbI} . The location of defects is marked with arrows. The calculations include SOC.

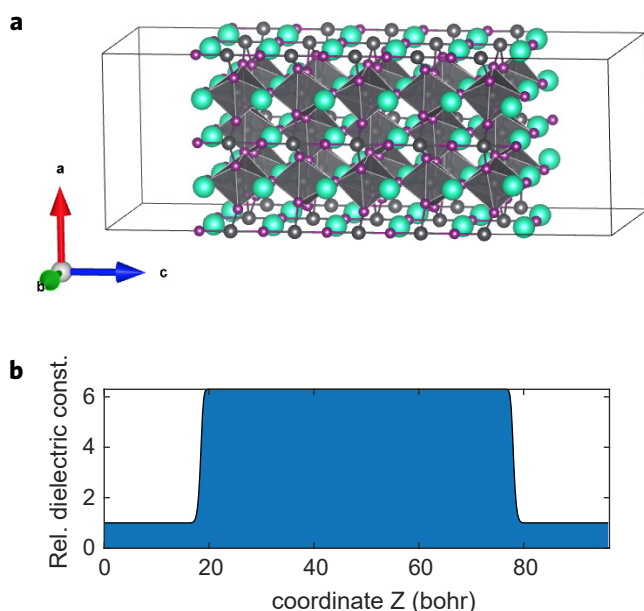


Figure S8: Effective dielectric model used in the evaluation of a correction for periodic charged slabs of tetragonal CsPbI₃: (a) Periodic slab structure. (b) Dielectric profile.

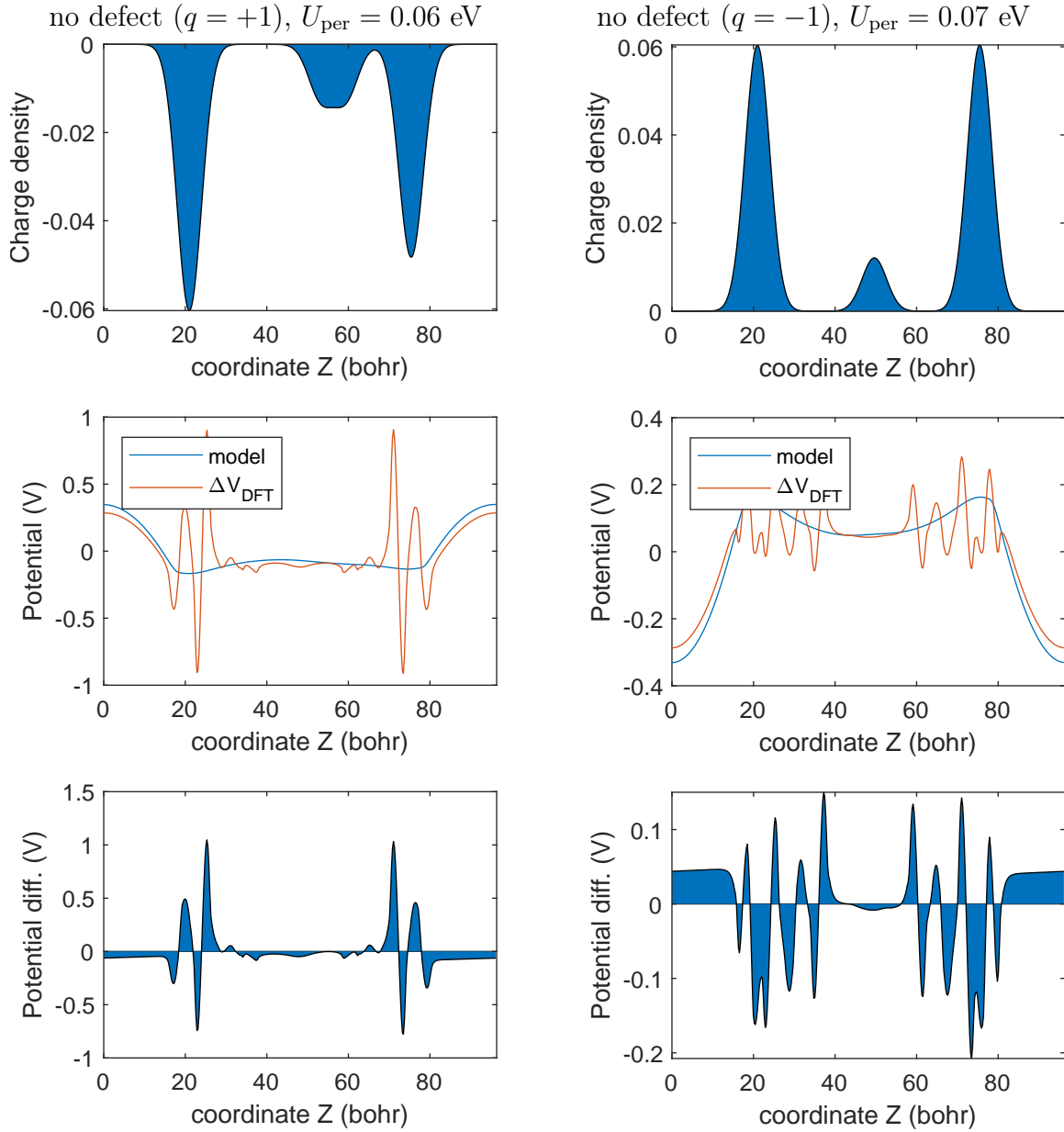


Figure S9: Output of `sxdefectalign2d` for an electrostatic model used in the evaluation of a correction for periodic charged slabs of tetragonal CsPbI_3 with and without defects and the excess charge q delocalized in the lateral plane: (top) Linear charge density distribution $\delta\rho(z)$. (middle) Model potential profile $\delta\phi(z)$ and the DFT potential $\Delta V_{\text{DFT}}(z)$. (bottom) Potential difference $\Delta V_{\text{DFT}} - \delta\phi$. SOC is not included.

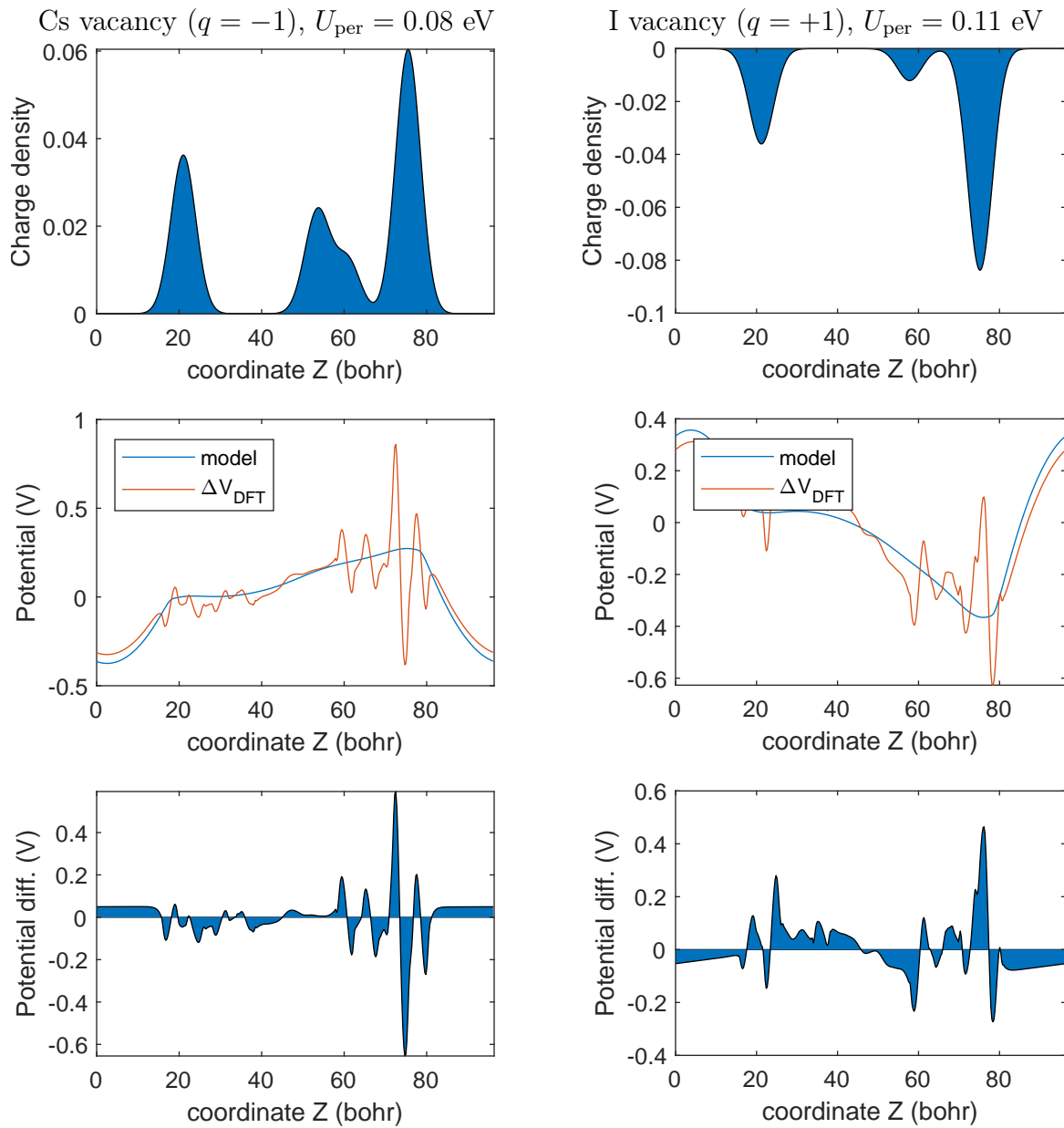


Figure S9: (continued)

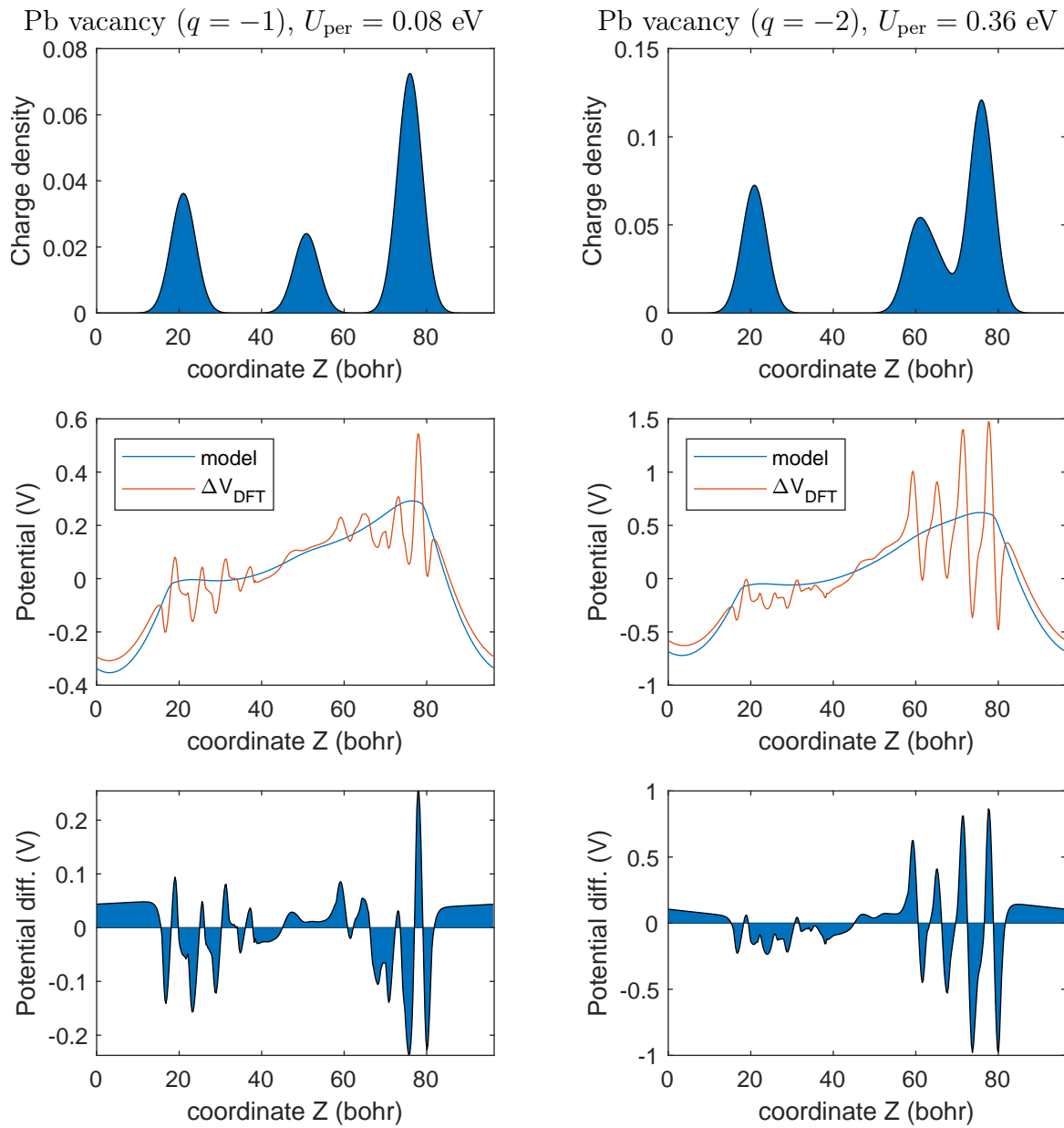


Figure S9: (continued)

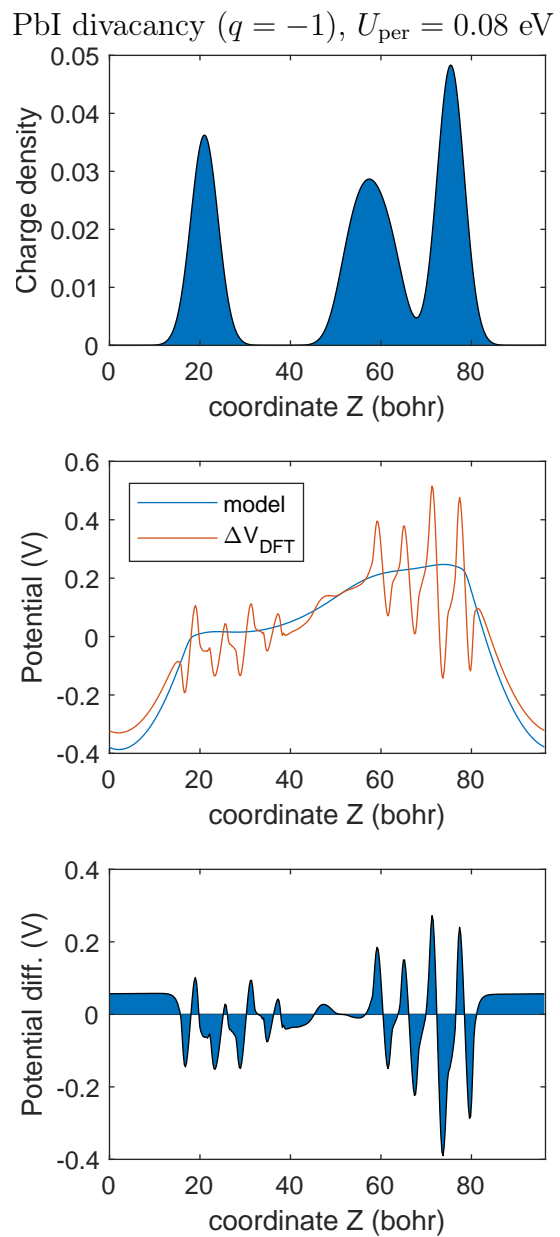


Figure S9: (continued)

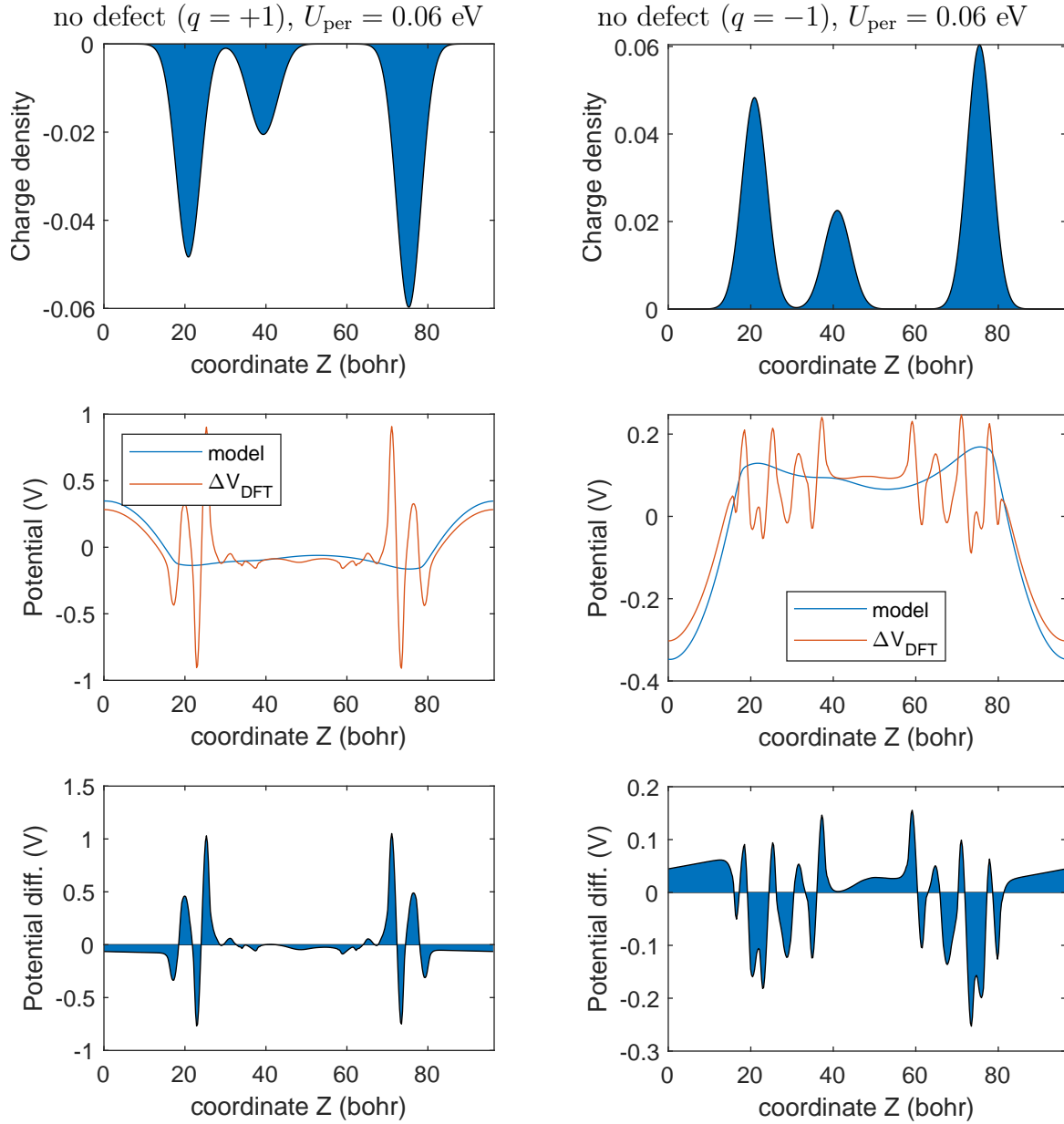


Figure S10: Output of `sxdefectalign2d` for an electrostatic model used in the evaluation of a correction for periodic charged slabs of tetragonal CsPbI_3 with and without defects and the excess charge q delocalized in the lateral plane: (top) Linear charge density distribution $\delta\rho(z)$. (middle) Model potential profile $\delta\phi(z)$ and the DFT potential $\Delta V_{\text{DFT}}(z)$. (bottom) Potential difference $\Delta V_{\text{DFT}} - \delta\phi$. SOC is included.

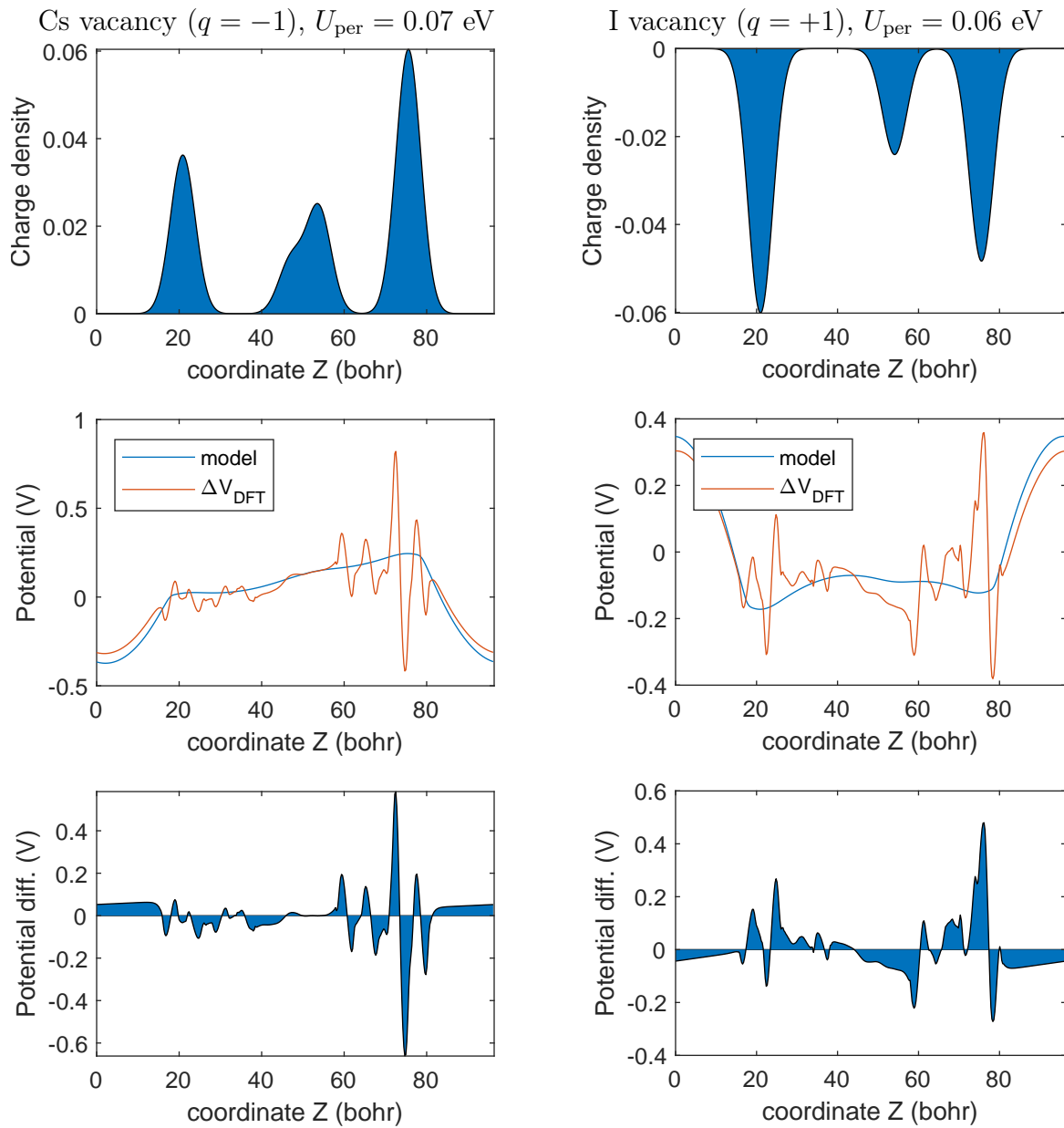


Figure S10: (continued)

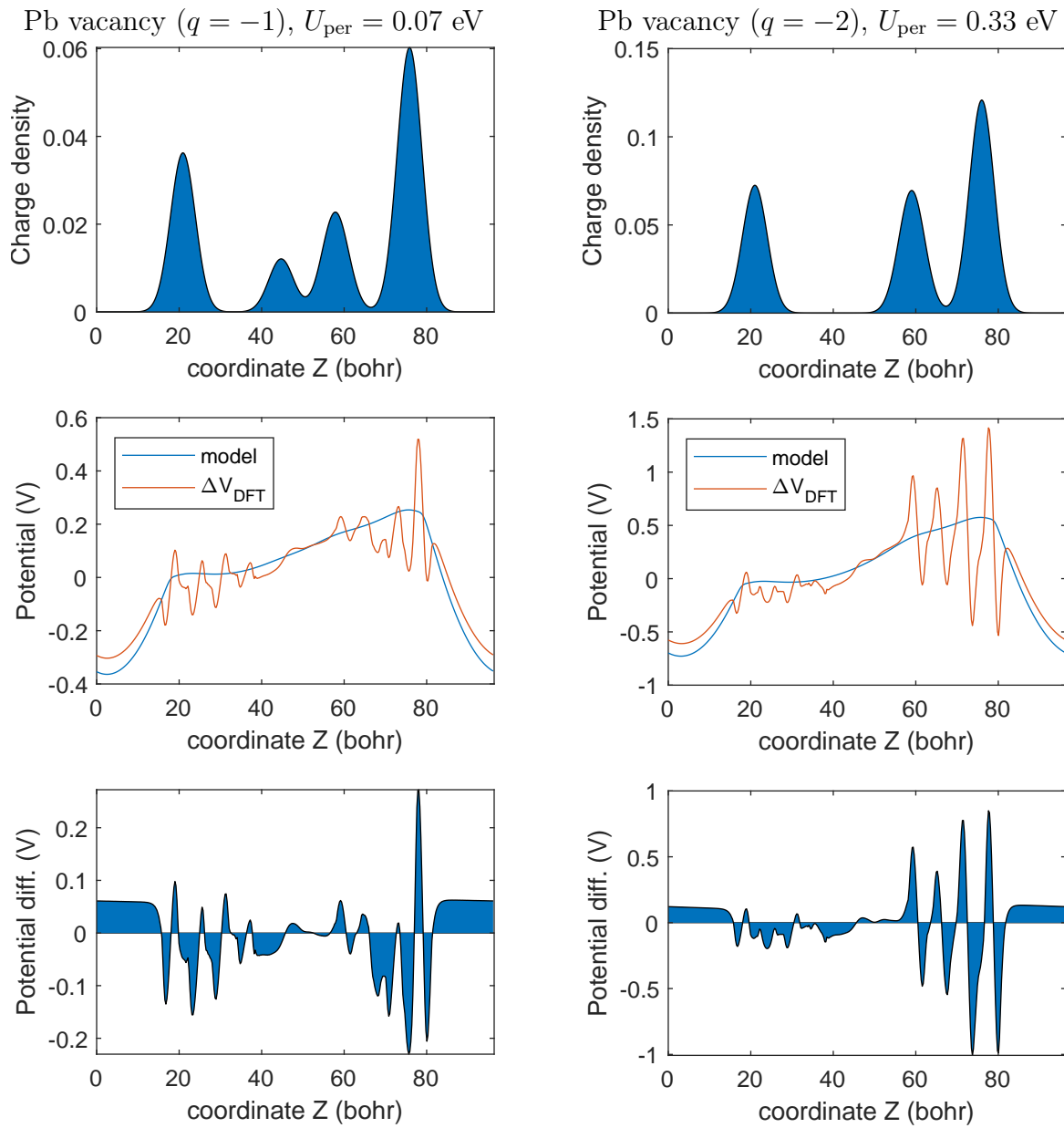


Figure S10: (continued)

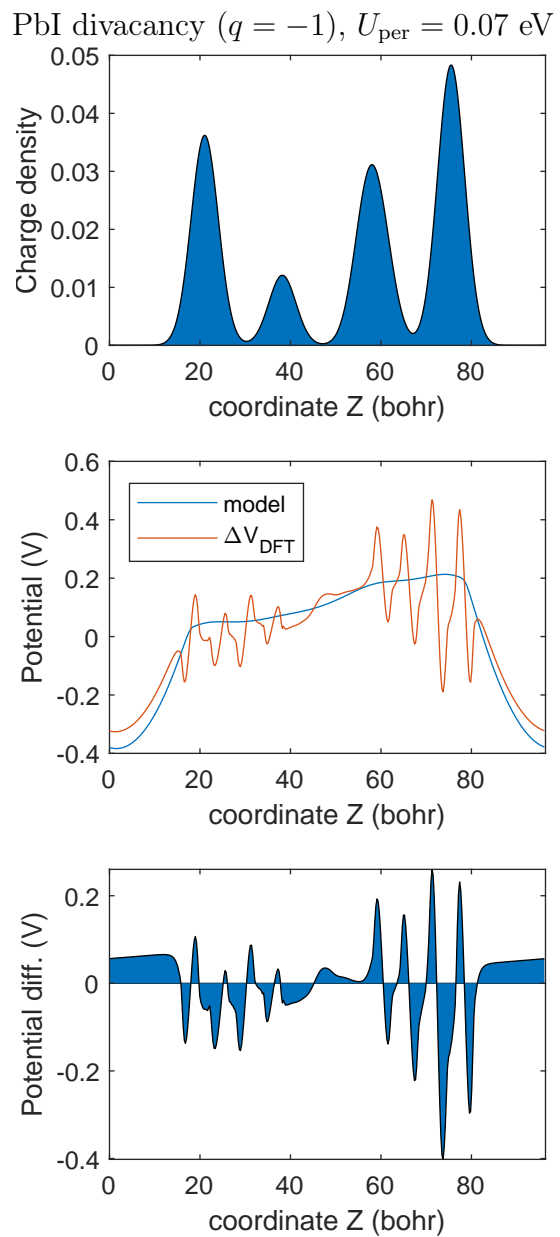


Figure S10: (continued)

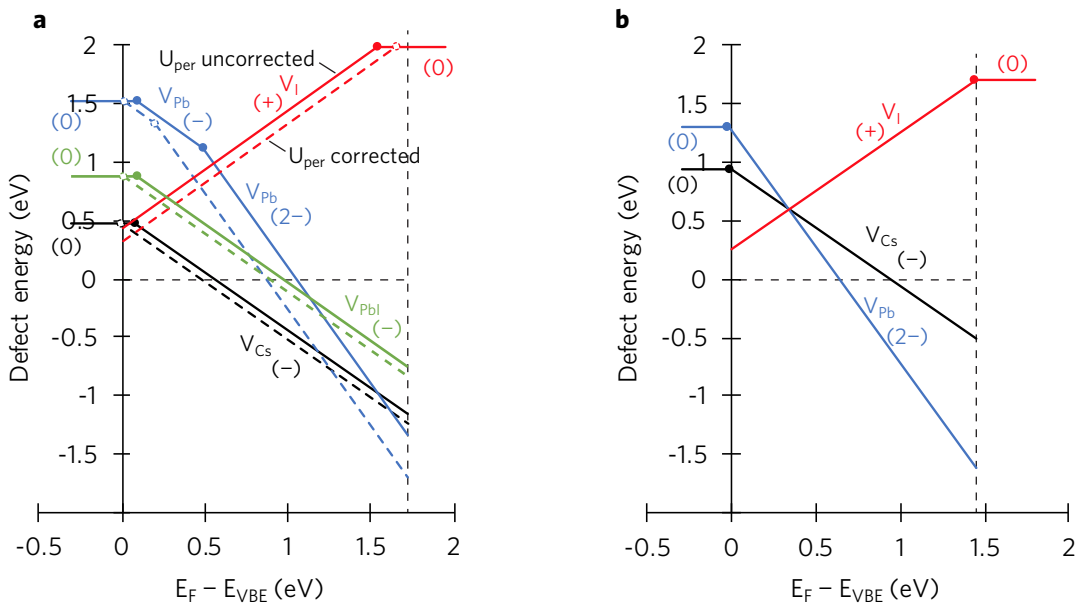


Figure S11: Formation energy of vacancies at the surface (a) and in the bulk (b) of tetragonal CsPbI₃ as a function of the Fermi energy (E_F). Values in brackets represent the charge state. The vertical dashed lines mark the location of the CBE. The chemical potential of elements is tuned to reflect solution-processed synthesis conditions. Results are shown without SOC to compensate for the DFT band gap error. Panel (a) presents data with and without the electrostatic correction U_{per} for charged defects in periodic slabs.

TOC Graphic

